Supporting Information

A flexible micro-thermoelectric device from carbon nanotube-epitaxially grown $(Bi,Sb)_2Te_3$ nanocrystal

Qun Jin[1,2], *Yang Zhao*[1,3], *Xuehao Long*[4], *Song Jiang*[1,2], *Ziqiang Wang*[4,5], *Pengyan Mao*[1,3], *Xiaoqi Li*[1,3], *Kan Cui*[1,3], *Jianhang Qiu*[1,3], *Ye Wan*[6], *Kaiping Tai*[1,3,7]*, *Ning Gao*[4,8]*, *Jun Tan*[7]*, *Chang Liu*[1,3]*, *Hui-Ming Cheng*[1,9]

[1] Shenyang National Laboratory for Materials Science, Institute of Metal Research, Chinese Academy of Sciences, Shenyang, China.

[2] University of Chinese Academy of Sciences, Shenyang, China.

[3] Department of Materials Science and Engineering, University of Science and Technology of China, Shenyang, China.

[4] Institute of Frontier and Interdisciplinary Science and Key Laboratory of Particle Physics and Particle Irradiation (MOE), Shandong University, Qingdao, China.

[5] Key Laboratory of Bionic Engineering Ministry of Education, Jilin University, Changchun, China.

[6] School of Materials Science and Engineering, Shenyang Jianzhu University, Shenyang, China.

[7] Ji Hua Laboratory, Advanced Manufacturing Science and Technology Guangdong Laboratory, Foshan, China.

[8] Institute of Modern Physics, Chinese Academy of Sciences, Lanzhou, China.

[9] Shenzhen Institute of Advanced Technology, Chinese Academy of Sciences, Shenzhen, China.

*Corresponding authors

E-mails: kptai@imr.ac.cn; ning.gao@sdu.edu.cn; tanjun@jihualab.com; cliu@imr.ac.cn

This file includes:

Contents

Supplementary Note 1 | Computational simulation methods

Different computational models were built to compare with the experimental results in this work. The SWCNTs with a bundle structure were built by rolling up single graphene along the armchair direction[1], as shown in Supplementary Fig. 8. Since it is not obvious that the chiral angle of SWCNT has any impact on the growth of the nanocrystals according to our experimental results, all the SWCNTs used in the computational studies were armchair-type tubes. The electronic structure of SWCNTs is similar to that of a graphene sheet where each carbon atom has three sp^2-hybridized electrons, forming strong covalent σ-bonds with the nearest neighbors, and a nonhybridized electron in p_z-orbitals, forming the weaker delocalized π-bonds which has a key influence on the electronic properties of SWCNTs[2]. Due to the curvature of the SWCNTs, the lengths of C-C bonds and the direction of p_z-orbitals are different from the case of a graphene sheet. Furthermore, grooves with unique properties are formed between neighboring SWCNTs in a bundle (Supplementary Figs. 9-11), and these are expected to have strong interactions with the deposited atoms[3].

In this work, the diameter of SWCNTs is ~1.6 nm, which is similar to the actual value. The deposited nanocrystals contained tens to one hundred atoms and were initially located around one groove of SWCNT bundle to build the SWCNT bundle-nanocrystal computational model. Geometrical optimization and *ab initio* molecular dynamics (AIMD) simulations were carried out for SWCNT-nanocrystal systems using the CP2K program as described in Supplementary Note 2. CP2K is an open-source software to perform atomistic simulations and provides a general framework for different modeling methods such as Density Functional Theory (DFT) using mixed Gaussian and plane waves approaches[4]. It has higher precision than the Molecular Dynamics (MD) software (e.g. LAMMPS[5]) using a traditional empirical potential function and

a lower computational cost than other DFT software (e.g. Vienna Ab initio Simulation Package[6]). AIMD is an algorithm using forces obtained from accurate electronic structure calculations to generate the finite temperature MD trajectories in an accurate and unbiased way[7]. The total number of atoms used in the CP2K simulation was up to ~1,200. The time interval was 0.5 fs for AIMD and the maximum simulation time was up to 4.5 ps. The simulation temperature for AIMD relaxation was from 300 K to 800 K. Classical MD simulations were also performed for Sb_2Te_3 nanocrystals to calculate the lattice thermal conductivity and the flexibility as described in Supplementary Notes 7 and 11, by using the LAMMPS package[5] with a two-body interatomic potential[8]. The time interval was 1 ps for LAMMPS and the simulation temperature was from 270 K to 330 K.

Supplementary Note 2 | Epitaxial growth mechanism for the highly ordered microstructures

SWCNTs have unique electrical, thermal and mechanical properties and are a promising candidate for building high-performance hybrid materials. The deposited atoms preferentially nucleate at grooves in the SWCNT bundle and grow into nanocrystals. The preferred crystallographic growth orientation of a nanocrystal can be controlled by the deposition conditions (such as temperature, pressure, etc.), lowering the surface/interface energy. The $(Bi,Sb)_2Te_3$ alloy is a layer-structured TE material, consisting of quintuple Te_1-Bi (Sb)-Te_2-Bi (Sb)-Te_1 layers stacked perpendicular to the <000*l*> direction. The crystallographic orientations of the neighboring nanocrystals are well-aligned with the groove, and low-angle tilt boundaries are thus formed between them (Fig. 2). Such highly ordered microstructures can only be obtained at a temperature higher than ~600 K so that the deposited Bi-Sb-Te atoms have enough energy to overcome diffusion barriers and grow into energetically favorable crystal orientations and microstructures.

To explain the experimental observations, a SWCNT-$(Bi,Sb)_2Te_3$ system was computationally simulated (Supplementary Fig. 9). After structural relaxation, we see that the $(Bi,Sb)_2Te_3$ nanocrystals deposited on the surface of the SWCNT bundle always keep their bottoms away from the SWCNT surface with a separation distance greater than ~0.3 nm in all computational simulations. This distance is larger than the typical chemical bond length (~0.2 nm) between a deposited atom and a SWCNT, but close to the typical van der Waals (vdW) distance (~0.33 nm) between carbon nanotubes[9]. The electronic density calculations clearly show that no structural or chemical bond is formed between the $(Bi,Sb)_2Te_3$ nanocrystal and SWCNT bundle, even at the groove region (Supplementary Fig. 9). Therefore, both the

computational and experimental results indicate that the periodic distribution of vdW interactions along the CNT axis may play an important role in determining the growth of the $(Bi,Sb)_2Te_3$ nanocrystals to form highly ordered microstructures along the 1D SWCNT bundle axis. The geometry of the SWCNT bundle results in a periodic distribution of vdW forces around the SWCNTs grooves along the axis, as shown in Supplementary Fig. 10. We see that the groove region has lower energy for deposited atoms and nanocrystals compared with other regions on the SWCNT surface (Supplementary Fig. 11), indicating the SWCNT groove has a strong vdW interaction with the deposited atoms.

The energy of the SWCNT-Bi_2Te_3 nanocrystal hybrid with different orientations was calculated using CP2K software. These calculated results are not influenced by Bi/Sb substitution. It was found that the SWCNT-(000*l*) Bi-Te atomic plane has the minimum surface energy compared with the $(1\bar{1}00)$, $(01\bar{1}5)$ and $(01\bar{1}10)$ orientations, as shown in Supplementary Fig. 12. These results suggest that the Bi_2Te_3 nanocrystal deposits on the SWCNT bundle with the (000*l*) atomic plane parallel to the top surface of the bundle, forming an energetically favorable crystal orientation. The underlying mechanism is determined by the intrinsic properties of Bi_2Te_3 nanocrystal[10]. Furthermore, the dependence of the total energy of the SWCNT-Bi_2Te_3 nanocrystal on the rotation angle of the Bi_2Te_3 nanocrystal along the <000*l*> direction has also been calculated (Fig. 2f). The results suggest that the most stable state is for the deposited Bi_2Te_3 nanocrystal to have its $<1\bar{2}10>$ direction parallel to the SWCNT axis, which is consistent with the experimental results.

Based on these results, we see that the nanocrystals nucleate at the SWCNT bundle groove and are highly aligned with a specific orientation parallel to the SWCNT axis by a strong

SWCNT-nanocrystal vdW interaction, to achieve a minimum energy state. There is therefore a specific crystallographic orientation of the nanocrystals parallel to the SWCNT bundle grooves held there by vdW forces to minimize the free energy. Furthermore, it is shown that due to a long-range periodic vdW interaction, the SWCNT bundle can be generally used to guide the epitaxial growth of various nanocrystals with highly ordered microstructures, such as Pt, Au, Cu, Si, etc. (Supplementary Figs. 1-7). The static energy of truncated polyhedral Pt nanocrystals with different orientations and different positions relative to a SWCNT was also investigated and the results are shown in Supplementary Fig. 11. They show that the total energy of the system decreases to achieve a stable state as the Pt nanocrystal gets closer to the SWCNT groove region, and a truncated polyhedral Pt nanocrystal with its <100> direction aligned with the SWCNT axis/groove gives the minimum energy state. These results and analysis are clearly compatible with the experimental observations (Supplementary Fig. 3).

In contrast, the conventional approach for epitaxial growth using a 2D substrate requires a small lattice mismatch and an atomically flat surface, and thus extremely limits the kind and quality of epitaxial nanostructures[9]. Our results show that at a suitable deposition temperature, the deposited atoms have enough energy to overcome the barrier for rearrangement and diffusion, resulting in the epitaxial growth of nanocrystals with a specific crystallographic orientation.

Supplementary Note 3 | Epitaxial growth of the SWCNT-$(Bi,Sb)_2Te_3$ hybrid

At the beginning of the deposition, the Bi-Sb-Te atoms reach the surface of SWCNTs (Supplementary Fig. 13) and epitaxially nucleate at a bundle groove by a strong vdW interaction[11,12] and the neighbouring nuclei merge into larger ones through surface diffusion. The nanocrystals are individually and separately anchored on the SWCNT scaffold, indicating that the early deposited atoms preferentially aggregate to grow into nanocrystals rather than occupying the bare surface of the SWCNT bundle (Fig. 2a). Most of the nanocrystals have very similar hexagonal morphology of nanosheets and have an in-plane size of hundreds of nanometers and a thickness of a few nanometers (Supplementary Fig. 14). The long edge of each nanosheet is parallel to the local axis/groove of the SWCNT bundle (Fig. 2a-c), indicating fast diffusion and the growth direction[13]. All the hexagonal atomic planes appear to be approximately perpendicular to the e-beam in the SEM/TEM (Fig. 2g,h), suggesting a preferred crystallographic orientation with minimum free energy. As shown by the SEM and TEM analysis, the hexagon is the $(Bi,Sb)_2Te_3$ (000*l*) atomic plane (Fig. 2a,b), which is approximately parallel to the hybrid free surface. With the growth of the $(1\bar{2}10)$ atomic plane, the nanosheet gradually covered the whole SWCNT bundle (Fig. 2a). With increasing deposition time, Bi-Sb-Te atoms are stacked on the formed (000*l*) atomic plane to make it thicker, forming a flat surface with an atomic-level height step edge (Fig. 2d and Supplementary Video 1). After ~40 minutes of deposition, the thickness of the hybrid had increased to ~720 nm and the spaces in the SWCNTs network could not be fully filled by the depositing atoms, forming irregular and randomly distributed nanopores between the nanocrystals. Supplementary Fig. 15 shows X-ray diffraction (XRD) patterns of the deposited hybrid, and the characteristic diffraction peaks can be indexed to rhombohedral $(Bi,Sb)_2Te_3$ (JCPDS no. 49-1713). The orientation factors *F* of the

182 hybrids were calculated using Lotgering's method[12,14] and are given in Supplementary Table 1.

183 The $Bi_{0.5}Sb_{1.5}Te_3$ nanocrystals have a strong out-of-plane (000*l*)-texture, consistent with the

184 SEM and TEM analyses (Fig. 2 and Supplementary Fig. 1).

Supplementary Note 4 | Thermoelectric properties of SWCNT-$(Bi,Sb)_2Te_3$ hybrids

The in-plane electrical conductivity (σ) values of all samples decrease with increasing temperature, showing a degenerate semiconductor behaviour. The σ values of the hybrids are lower than those of the dense film and the σ value of (000*l*)-textured hybrid is higher than that of the non-textured one (Fig. 3a). The carrier concentration (n) and carrier mobility (μ) values of samples with different Bi:Sb ratios are shown in Supplementary Fig. 16. In the hybrids, n rapidly increases with the decreasing mole content of Bi atoms and the μ values change inversely which could be because of the increase of Sb_{Te} antisite defects[15]. Although the contribution of SWCNTs to the TE performance is limited (Supplementary Figs. 17 and 18), the SWCNTs play an important role in guiding the highly ordered growth[11] of the freestanding hybrid with unique microstructures that cause little carrier scattering and suppress the phonon transport[16]. The TE properties of the hybrids were tested at 370 K for ~120 h (Supplementary Figs. 19 and 20) to evaluate their long-term durability, and almost no change was observed in the Seebeck coefficient (α) and σ values, indicating good thermal stability. All the in-plane α values are positive (Fig. 3b), indicating p-type hole carrier conduction. α reaches a maximum value at ~390 K, because of the bipolar effect[17]. The SWCNT is an intrinsic n-type semiconductor[18] and the deposited $(Bi,Sb)_2Te_3$ is p-type. When the $(Bi,Sb)_2Te_3$ nanocrystals are attached to the SWCNTs, p-n heterojunctions are formed at the interfaces, which could consume the hole carriers and result in a decrease of n. Although the volume fraction of the SWCNTs is as low as ~1.4%, the $(Bi,Sb)_2Te_3$/SWCNT interfacial area is large because of the very small diameter of the nanotubes. Because of the misalignment between their band structures, there could be a band bending effect at the $(Bi,Sb)_2Te_3$/SWCNT interface. The carriers would generally suffer energy-dependent scattering at the interface because of the

208 bending potential[19,20], which could lead to an increase in α. However, the α values of the hybrid
209 are close to that of dense film, indicating the interfacial effect on filtering out low-energy
210 electrons is weak in the hybrid, consistent with the changes in α (Fig. 3b) and μ (Supplementary
211 Fig. 16).

Supplementary Note 5 | Scattering parameter estimation based on the Pisarenko expression

Assuming a simple parabolic electronic band structure for degenerate semiconductors, the relationship between α and n values can be estimated by the following formula[21-23]:

$$\alpha = \frac{8\pi^2 k_B^2 m^* T}{3eh^2} \cdot \left(\frac{\pi}{3n}\right)^{\frac{2}{3}} \cdot (1+r) \quad \text{(S1)}$$

where m^* is the carrier density-of-states effective mass, and r is the scattering parameter. Although the calculation may not be accurate due to the complicated scattering processes and the non-parabolic behavior of the conduction band of Bi_2Te_3-based alloys[24], the relationship between $|\alpha|$, r and m^* can be approximately described by this formula[25-27]. The m^* of the hybrid cannot obviously be changed by the SWCNTs because of their low volume content. Therefore, based on the above expression and the measured $|\alpha|$ and n values of the hybrids and a dense $Bi_xSb_{2-x}Te_3$ film (Supplementary Fig. 16), their scattering parameter values can be calculated. Assuming the charge carriers are predominantly scattered by acoustic phonons, the ratio of scattering parameter values for the dense $Bi_{0.5}Sb_{1.5}Te_3$ film (n_1), and the ~720-nm-thick $Bi_xSb_{2-x}Te_3$-SWCNT hybrids with different Bi doping levels (x = 0.3, 0.4, 0.5, 0.55; $n = n_2$, n_3, n_4, n_5) can be expected to be given by the measured Seebeck coefficients and carrier concentrations based on the above equation:

$$(\alpha_1 \cdot n_1^{\frac{2}{3}}) : (\alpha_2 \cdot n_2^{\frac{2}{3}}) : (\alpha_3 \cdot n_3^{\frac{2}{3}}) : (\alpha_4 \cdot n_4^{\frac{2}{3}}) : (\alpha_5 \cdot n_5^{\frac{2}{3}}) = (1+r_1):(1+r_2):(1+r_3):(1+r_4):(1+r_5) \quad \text{(S2)}$$

Based on the measured α and n values, the scattering parameter values for the hybrids and dense $Bi_xSb_{2-x}Te_3$ film are calculated to be approximately equal, implying that the SWCNTs have little influence on the carrier scattering mechanism of the hybrid, which is in good agreement with the analysis of the fitted electrical conductivity (Supplementary Fig. 16).

Supplementary Note 6 | Calculation of thermal conductivity contribution

To reveal the underlying mechanism for the reduced thermal conductivity of the hybrid, the lattice (κ_l^h), electron (κ_e^n) and bipolar (κ_b^h) thermal conductivities were calculated using the Wiedemann-Franz relationship. $\kappa_l^h+\kappa_b^h = \kappa_{tot} - \kappa_e^n$, $\kappa_e^n = L \cdot \sigma \cdot T$, where L is the Lorenz number. The estimate of the Lorenz number is based on the measured Seebeck coefficient[28]: L=1.5+exp (−|S|/116) (where L is in units of 10^{-8} W Ω K^{-2} and S in μV K^{-1}). It was found that the $\kappa_l^h+\kappa_b^h$ values are smaller than those of a dense film[29,30], and slightly increase with increasing temperature (Supplementary Fig. 21b) due to an increase of the κ_b^h effect[17]. The contributions of phonons with different mean free paths to κ_l were recently calculated for the Bi_2Te_3-based alloys[31]. In the $(Bi,Sb)_2Te_3$ alloy, the phonons with mean free paths shorter than ~200 nm make more than a ~95% contribution to the total κ_l (ref. [32]). Therefore, multiscale defects, including point defects, dislocations, grain boundaries, stacking faults, twin boundaries, pore boundaries, interfaces, etc., that are of the same or a smaller size strongly scatter the phonon transport, substantially decreasing the lattice thermal conductivity. Such structures may therefore produce a highly decreased κ_l. The phonons in the hybrid have a wide range of wavelengths and are scattered by the combined effect of many different multiscale defects. Phonons with a short-wavelength are mainly scattered by the short-range intrinsic defects, such as point defects, dislocations, stacking faults, twin boundaries, etc.; the phonons with mid-to-long wavelength are strongly scattered by the long-range defects, such as the $(Bi,Sb)_2Te_3$/SWCNT interfaces, grain boundaries and pore boundaries etc. (ref. [31]). In the p-type $(Bi,Sb)_2Te_3$ alloy, the point defects of Sb_{Te} and Bi_{Te} antisites or V_{Sb} and V_{Bi} vacancies are the main reasons for the acceptor conduction behavior[15]. Because the carrier concentrations and average grain size in the (000*l*)-textured film and the hybrid are comparable[29,30], their influences

on phonon conduction are similar. Therefore, the nanoporous structure, the $(Bi,Sb)_2Te_3$/SWCNT interfaces and the randomly distributed, irregularly shaped nanopore boundaries in the hybrids could account for such ultralow lattice thermal conductivity[33]. The nanopores with large specific pore boundary areas scatter the phonons more effectively than the micropores[33], as illustrated in Fig. 1. The $(Bi,Sb)_2Te_3$/SWCNT interfaces also lower the lattice thermal conductivity without much effect on the electrical conductivity, which is demonstrated by modifying the interface structure using a plasma-treated SWCNT deposition matrix[16].

Supplementary Note 7 | MD simulation of the effect on the value of κ_l of grain boundaries with tilt angles

The thermal transport properties of Sb_2Te_3 nanocrystals with small and large tilt angle grain boundaries were calculated using the non-equilibrium molecular dynamics (NEMD) method in a large-scale atomic/molecular massively parallel simulator (LAMMPS). The Sb_2Te_3 models were constructed by combining two neighboring grains with a tilt angle (θ) of 0-30°, as shown in Supplementary Fig. 22. According to Fourier's law, the thermal conductivity κ is defined by the following equation:

$$J = -\kappa \nabla T \tag{S3}$$

where J is the heat flux in units of energy per area per time and ∇T is the spatial gradient of temperature. In this work, the kinetic energy is swapped between atoms in two different layers of the simulation box, which induces a temperature gradient between them. The transferred cumulative energy can also be obtained after full relaxation to calculate the heat flux. With the calculated heat flux and temperature gradient, the thermal conductivity κ can be obtained using the above equation. During the relaxation, a free boundary condition was applied along all directions. The pair potential was applied for the Sb_2Te_3 nanocrystals since there is no suitable ternary empirical potential function for the $(Bi,Sb)_2Te_3$ system. The underlying mechanism of the effect of grain boundaries on phonon transport and lattice thermal conductivity should be the same in Sb_2Te_3 and $(Bi,Sb)_2Te_3$ alloys.

After minimizing the energy of the system using the conjugate gradient method, the simulation system was then relaxed using a canonical ensemble at 300 K for 20 ps, followed by further relaxation at 300 K using the microcanonical ensemble for another 20 ps. The temperature distribution was then changed by adding and subtracting the thermal energy from

the hot and cold regions at the two ends of the model, respectively, at a constant rate by velocity scaling along the <1$\bar{2}$10> direction under total energy conservation. The region containing grain boundaries was located at the center of the computational box along the <1$\bar{2}$10> direction in order to avoid the influence of the artificial addition and removal of thermal energy.

After full relaxation, the temperature gradient was then determined, as shown by the inset image in Supplementary Fig. 22b. Following the method provided in ref. [34], the generated temperature distribution curve along the y axis was then obtained. The lattice thermal conductivity of Sb_2Te_3 nanocrystals was calculated using the following formula:

$$\kappa = \frac{Q}{t} \times \frac{L}{A \cdot \Delta T} \tag{S4}$$

where κ is the thermal conductivity in W/(m·K), Q is the amount of heat transferred through the material in Watts, L is the distance between the two isothermal planes, A is the area of the surface that is perpendicular to the heat transfer direction in square meters, and ΔT is the temperature difference in Kelvin. Following the above method, it is clear that for the heat transfer process of Sb_2Te_3 models containing different grain boundaries, only the ΔT value is different. Therefore, the normalized thermal conductivity (κ_{norm}) of a Sb_2Te_3 nanocrystal with grain boundaries formed by rotating one grain along [000l] by different angles, θ, can be calculated by comparison with a nanocrystal without grain boundaries:

$$\kappa_{norm} = \frac{\kappa_\theta}{\kappa_0} = \frac{\Delta T_\theta}{\Delta T_0} \tag{S5}$$

The results shown in Supplementary Fig. 22c clearly show that the lattice thermal conductivity of Sb_2Te_3 nanocrystals is strongly impacted by grain boundaries even with small tilt angles.

Supplementary Note 8 | Calculation of the P_c, COP, Q, P_g, power density values of a micro-TED

The internal electrical resistance (R) of the micro-TED module consists of the electrical resistance of the two p-n couples ($R_{p\text{-}n}$), the Pt leads (R_{lead}) and the contact resistance ($R_{contact}$) between the p-n couples and the Pt leads. $R_{p\text{-}n}$ is ~130 Ω, as measured by a four-probe technique, and R is ~258 Ω at RT determined by applying a voltage and measuring the electric current through the whole micro-TE module. Because the p- and n-type hybrids have different thermal and electrical conductivities, the p- and n-leg are designed with different dimensions to optimize the n-p couple TE performance. The p and n couples both have dimensions of ~50 μm wide (W), ~50 μm long (L) and ~0.72 μm (D_p) and 0.65 μm (D_n) thick (Fig. 4a). The maximum cooling power P_c^{max} of a TE module including two (N = 2) p-n couples is defined as the maximum cooling ability at a temperature difference of zero (ΔT=0 K) across the module and can be estimated by the following equation[35]:

$$P_c^{max} = N \times (S_{p\text{-}n} T_c I_{max} - 0.5 \times I_{max}^2 R) \quad \text{(S6)}$$

where $S_{p\text{-}n}$, R , I_{max} and T_c are the Seebeck coefficient, the electrical resistance, cooling current at the highest cooling effect and the temperature of the cold side of the TE module, respectively. Using the measured $S_{p\text{-}n}$, R and T_c values. The maximum cooling power density Q_c^{max} is estimated by dividing P_c^{max} by the total cross-sectional area (A_c) of the two p-n couples along the heat flow direction, as shown in Fig. 4c.

$$Q_c^{max} = \frac{P_c^{max}}{A_c} = \frac{P_c^{max}}{N \times W \times (D_p + D_n)} \quad \text{(S7)}$$

The COP values with the cooling current (I) at ΔT= 0 K are expressed by the following equation:

$$COP = \frac{(S_{p\text{-}n} T_c I - 0.5 \times I^2 R)}{I^2 R} \quad \text{(S8)}$$

For the micro-TEG, when the load resistance matches the TE module resistance, the maximum output electrical power (P_g^{max}) can be approximately estimated by the expression:

$$P_g^{max} = \frac{V^2}{4R} \tag{S9}$$

where V is the open circuit thermal voltage, R is the internal resistance of the TE module. The maximum output power density (Q_g^{max}) is estimated by dividing P_g^{max} by the total cross-sectional area (A_c) of the two p-n couples along the heat flow direction, as shown in Fig. 4g. Both P_c^{max} and P_g^{max} are inversely proportional to the R of the TE module and can therefore be improved by reducing the resistance of the TE module.

Supplementary Note 9 | Dependence of cooling ΔT on an applied current of micro-TEC

In a closed system, the dependence of net cooling on applied electrical current is caused by three primary competing mechanisms. First, the charge carriers carry heat from the target cooled area to the heat sink through the Peltier effect which varies linearly with the applied current. Second, the electrical current also heats the whole device by Joule heating because of the electrical resistance and this varies as the square of the current. There thus exists a certain current, at which the cooling power reaches its maximum value. When the electrical current is larger than a certain value, Joule heating dominates the heat balance and decreases the total cooling performance. Third, there is a cooling loss by thermal conduction from the TEC hot side to the cold side due to the temperature gradient.

Supplementary Note 10 | Estimation of the bending strain of the hybrid

When a deposited film and a compliant substrate have the same Young's modulus, the strain in the top sample (ε_{sample}) is as follows[36],

$$\varepsilon_{sample} = \frac{(d_{sample}+d_{substrate})}{2R} \quad \text{(S10)}$$

where the thickness and Young's modulus of the deposited film and substrate are d_{sample} and $d_{substrate}$, Y_{sample} and $Y_{substrate}$, respectively, and R is the bending radius. When the film and substrate have different moduli ($Y_{sample}>Y_{substrate}$), the neutral plane moves toward the more rigid film, and ε_{sample} is given by:

$$\varepsilon_{sample} = \frac{(d_{sample}+d_{substrate})}{2R}\frac{(1+2\eta+\chi\eta^2)}{(1+\eta)(1+\chi\eta)} \quad \text{(S11)}$$

$$\varepsilon_{sample} = 0.83\times\frac{(d_{sample}+d_{substrate})}{2R} \quad \text{(S12)}$$

where $\eta = d_{sample} / d_{substrate}$ and $\chi = Y_{sample} / Y_{substrate}$. Equations (S11) and (S12) provide the theoretical basis for evaluating the SWCNT-$(Bi,Sb)_2Te_3$/polyimide samples[37-40]. The equations allow us to obtain the approximate value of ε_{sample}, which for the freestanding SWCNT-$(Bi,Sb)_2Te_3$ couple with an average thickness (d) of p- and n-type hybrids, is given by:

$$\varepsilon_{sample} = \frac{d}{2R} \quad \text{(S13)}$$

The bending of the freestanding p-n couple could be driven by AFM, and a schematic and the relationship between strain and moving distance, are shown in Supplementary Fig. 25.

Supplementary Note 11 | MD simulation of the flexibility of highly ordered nanocrystals

The bending of Sb_2Te_3 nanocrystals with low and high angle tilt grain boundaries has been simulated using the LAMMPS code with the two-body interatomic potential developed by Prabudhya et.al., which has been successfully used in calculations of the thermal conductivity and mechanical properties of Sb_2Te_3 (ref. [8]). Considering the non-negligible size effect of the nanocrystals with low-tilt-angle grain boundaries, the AIMD method is not suitable because of the limit on the number of atoms in the calculation. Because of the lack of a precise ternary empirical potential function for $(Bi,Sb)_2Te_3$, only Sb_2Te_3 bending is simulated but the underlying bending mechanism should be the same. SWCNTs are not considered in this simulation because of their ultra-high flexibility and good interfacial adhesion force (no nanocrystals peel-off during the bending test). The results of Sb_2Te_3 coupled with the previous simulation studies for Bi_2Te_3 (ref. [11]) should indicate the underlying mechanisms of the crystallographic-orientation-dependent bending of $(Bi,Sb)_2Te_3$ nanocrystals.

Structural models used in our simulations are built using three neighboring Sb_2Te_3 nanocrystals with the same (000*l*) orientation (along the *Z* direction) as shown in Supplementary Fig. 26, corresponding to the (000*l*)-textured structure in our experimental samples. Two grain boundaries are formed between these three grains. Low (5°) and high (15°) angle tilt grain boundaries are generated between the neighbouring nanocrystals by rotating the middle one around the normal direction to the (000*l*) atomic plane (*Z*-axis) by the given angle. The total number of atoms used in the Sb_2Te_3 simulation model is up to ~54,000. Following the method reported in ref. [11], the system is first relaxed before bending is applied by adding forces along the positive *Z*-axis on atoms at the central bottom region of the middle grain, while forces along the negative *Z*-axis on atoms at the bottom of two side grains, as shown in Supplementary Fig.

26a. After each movement, the stress tensor is calculated to show the stressed state of the grain boundaries, especially to check whether the stress concentration has been formed.

For the <1$\bar{2}$10> -5° grain boundary model, the low-angle between two neighboring grains results in a smooth connection between them after relaxation. A stress concentration is only observed in the limited mismatched region, while the other matched region efficiently releases the in-plane stress/strain concentrations by the slight sliding of neighbouring Te_1-Te_1 layers connected by vdW force, as shown in Fig. 5c-e and Supplementary Fig. 26b. In contrast, for the <1$\bar{2}$10> -15° model, a larger mismatched region with significant stress concentrations prevents the atomic plane from sliding across the nanocrystals, resulting in discontinuous atomic displacements and the rearrangement of atoms at the grain boundaries. Different from the models of nanocrystals aligned along <1$\bar{2}$10> direction, a strong stress concentration and discontinuous atomic displacements are observed both at low-angle (5°) boundaries when the nanocrystals are aligned along the <1$\bar{1}$00> direction, indicating that <1$\bar{2}$10> is the easy sliding direction on the (000*l*) atomic plane.

The cyclic bending of Sb_2Te_3 nanocrystals with 5°, 15° and 30° tilt boundaries along the <1$\bar{2}$10> direction has been simulated at room temperature. First, external forces are applied on the nanocrystals as shown in Supplementary Fig. 26a to produce bending. The nanocrystals were then relaxed, and the bending-relaxation processes were repeated ~40 times. After the bending cycles, the low (5°) angle tilt boundaries almost returned to their initial states, while the microstructures of the region near the grain boundaries with high (15° and 30°) tilt angles were irreversibly changed. The yellow lines in Fig. 5f indicate the mismatch of (000*l*) atomic layers between the two neighboring nanocrystals with the low- and high-angle tilt boundaries.

Such distortions could substantially scatter the electron transport and decrease the electrical conductivity.

It is concluded that the nanocrystals in the (000*l*) orientation with a low tilt-angle grain boundary along the $<1\bar{2}10>$ direction have much better flexibility than others, such as nanocrystals in the $(01\bar{1}5)$ or (000*l*) orientations with a tilt boundary along the $<1\bar{1}00>$ direction. These results have clearly explained the reason for the excellent flexibility of $(Bi,Sb)_2Te_3$ nanocrystals deposited on bundles of SWCNTs with (000*l*) atomic plane and the alignment with their $<1\bar{2}10>$ direction parallel to the grooves in the bundle.

418 **Supplementary Fig. 1**

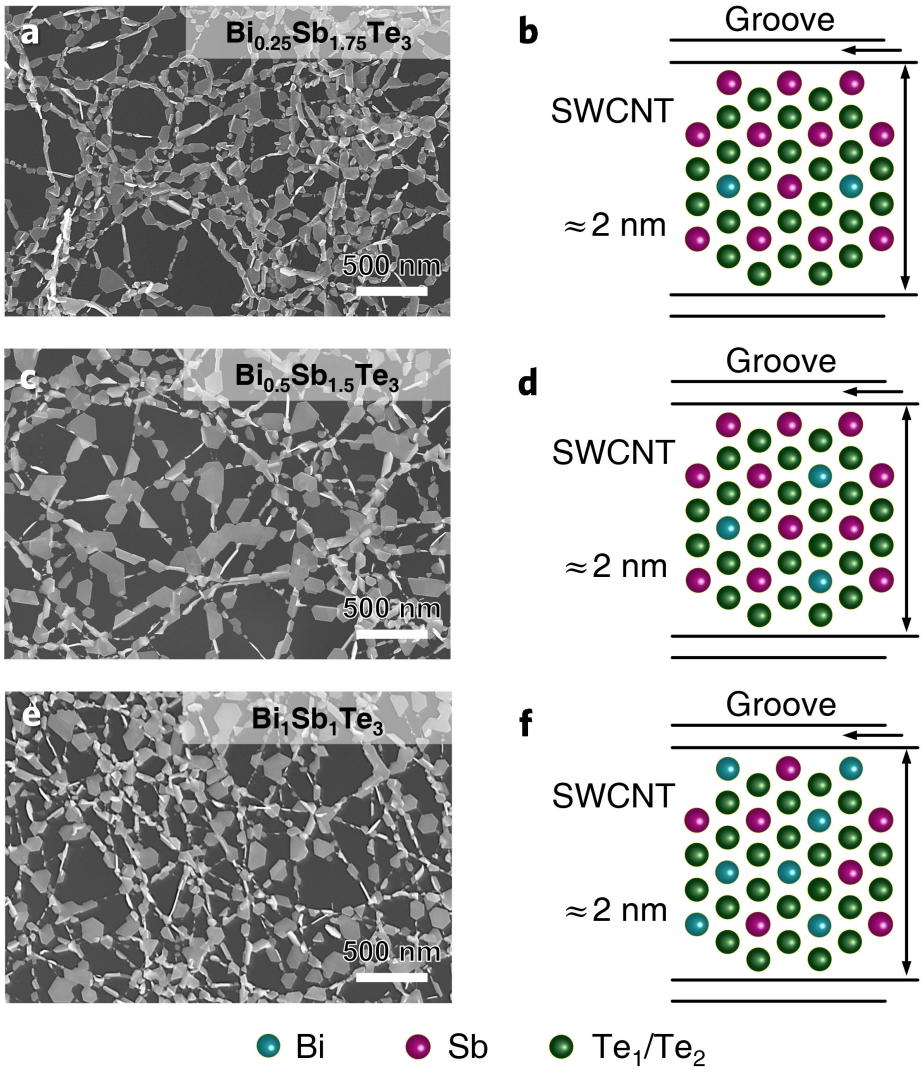

419

420 **Supplementary Fig. 1 | SEM images of highly ordered SWCNT-$Bi_xSb_{2-x}Te_3$ hybrids with**
421 **different Bi doping levels. a-b,** SWCNT-$Bi_{0.25}Sb_{1.75}Te_3$ hybrid and a schematic of the
422 orientation relationship. **c-d,** SWCNT-$Bi_{0.5}Sb_{1.5}Te_3$ hybrid and a schematic of the orientation
423 relationship. **e-f,** SWCNT-$Bi_1Sb_1Te_3$ hybrid and a schematic of the orientation relationship.

Supplementary Fig. 2

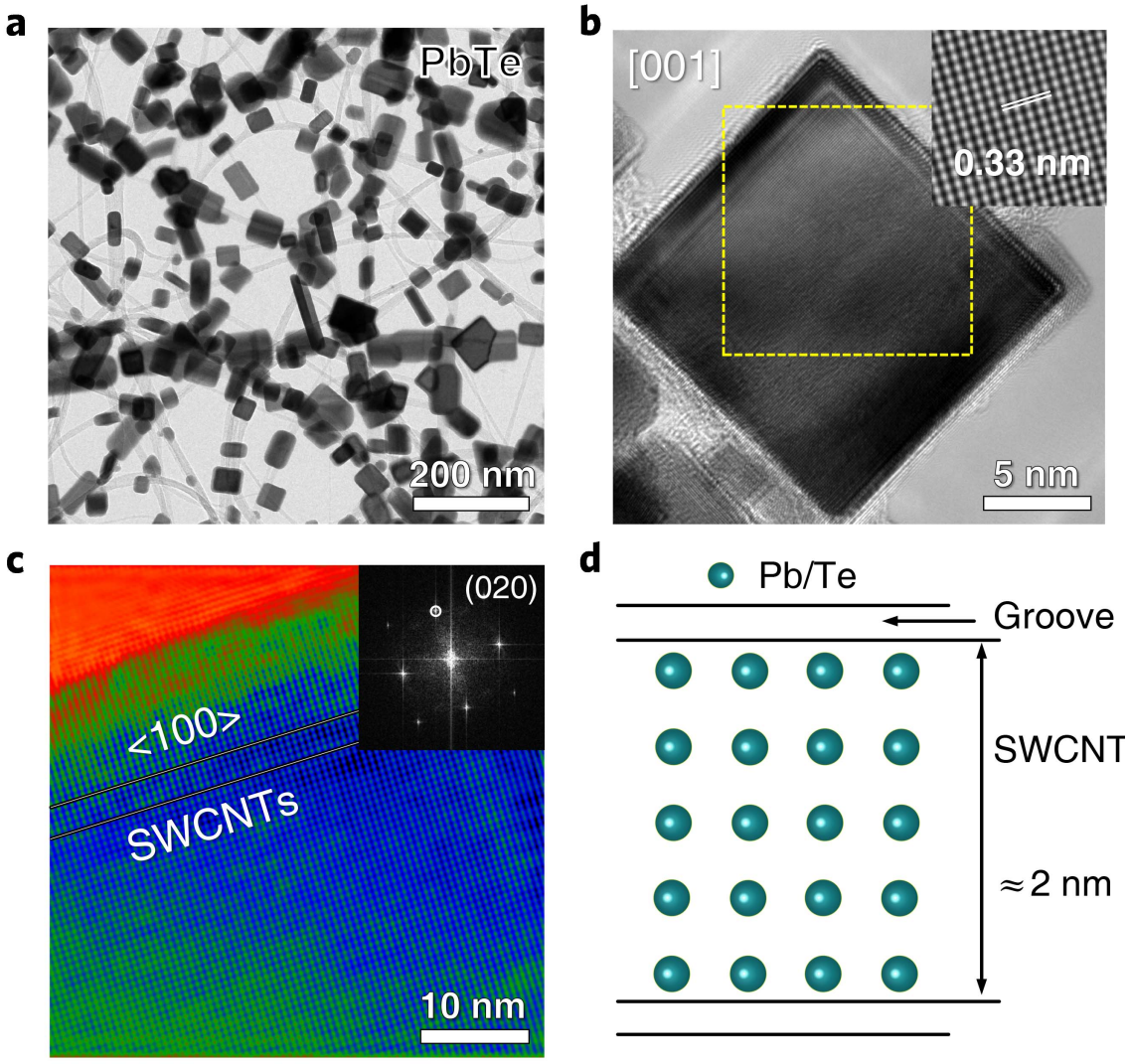

Supplementary Fig. 2 | a-b Bright-field TEM images of a highly ordered SWCNT-PbTe hybrid. Inset in **b** is the inverse-fast Fourier transform (FFT) image. **c,** False-color inverse-FFT image from the area outlined in **b**. Inset is the corresponding FFT. **d,** Schematic of the orientation relationship between PbTe and SWCNT.

Supplementary Fig. 3

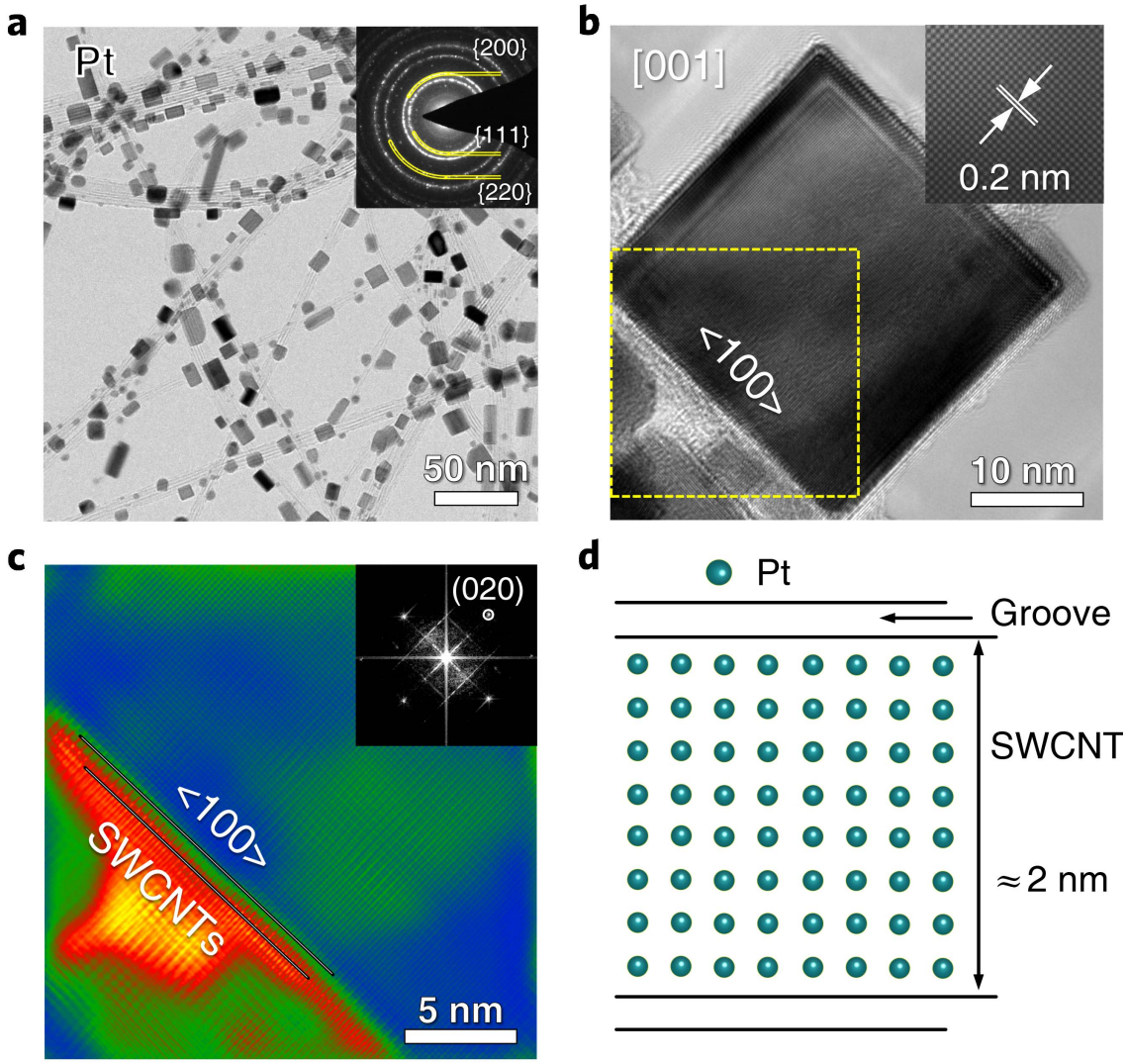

Supplementary Fig. 3 | a-b, Bright-field TEM images of a highly ordered SWCNT-Pt hybrid. Inset in **b** is the inverse-fast FFT image. **c,** False-color inverse-FFT image from the area outlined in **b**. Inset is the corresponding FFT. **d,** Schematic of the orientation relationship between Pt and SWCNT. Supplementary Fig. 3a is also shown in Fig. 2a.

436 **Supplementary Fig. 4**

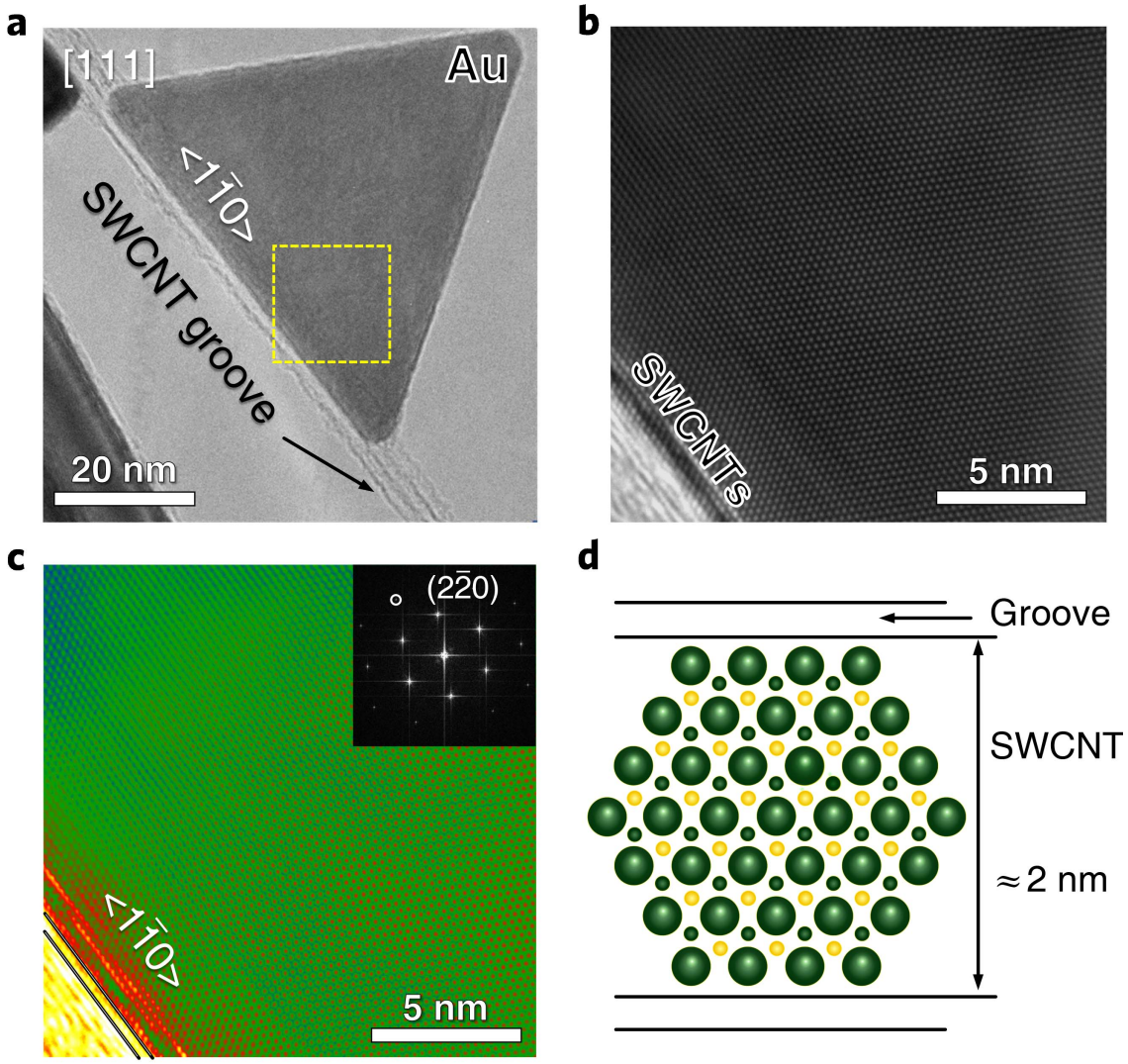

437

438 **Supplementary Fig. 4 | a-b, Bright-field TEM images of a highly ordered SWCNT-Au**
439 **hybrid.** Inset in b is the inverse-fast FFT image. **c,** False-color inverse-FFT image from the
440 area outlined in **b**. Inset is the corresponding FFT. **d,** Schematic of the orientation relationship
441 between Au and SWCNT.

Supplementary Fig. 5

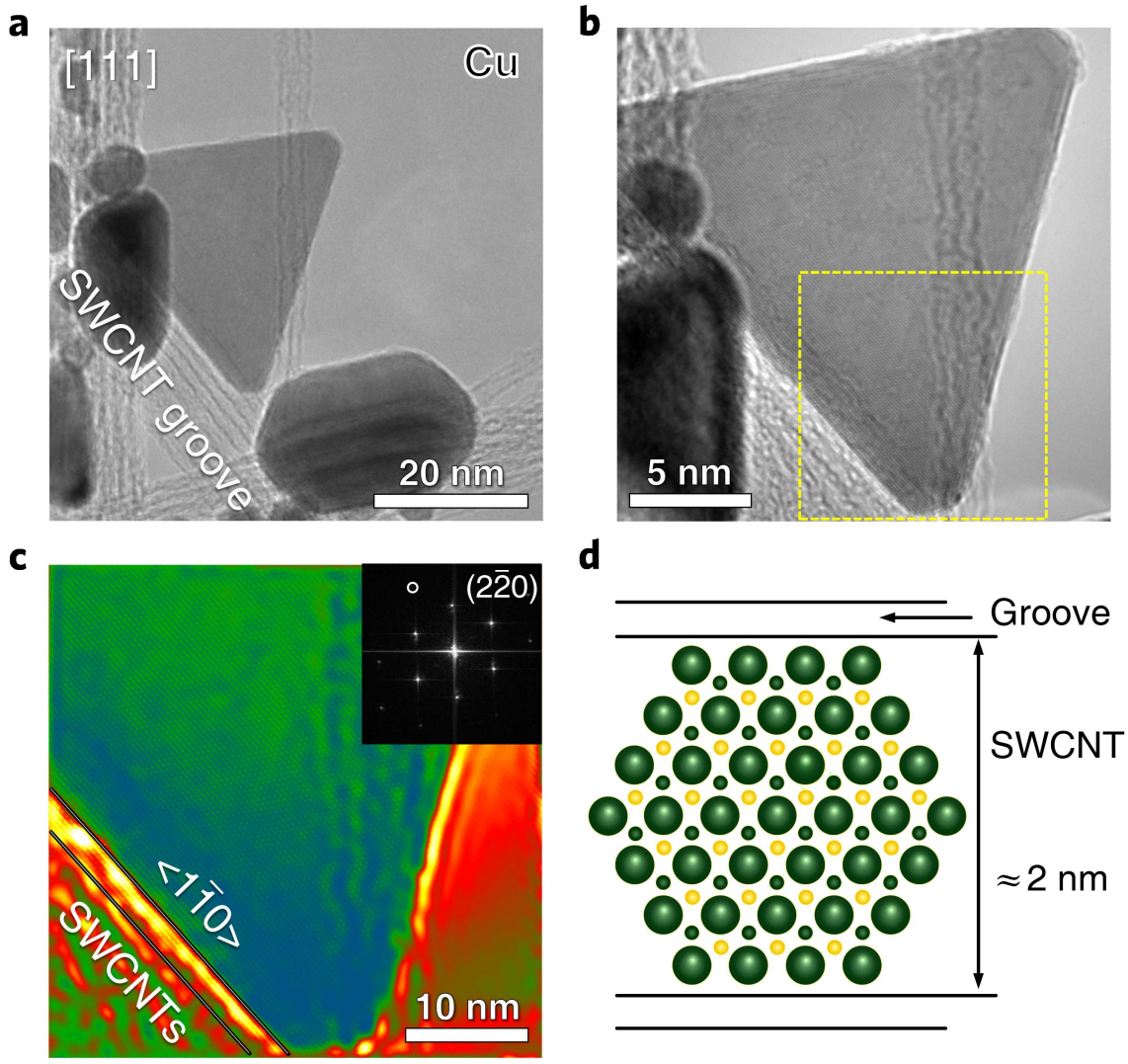

Supplementary Fig. 5 | a-b, Bright-field TEM images of a highly ordered SWCNT-Cu hybrid. Inset in b is the inverse-fast FFT image. **c,** False-color inverse-FFT image from the area outlined in **b**. Inset is the corresponding FFT. **d,** Schematic of the orientation relationship between Cu and SWCNT.

Supplementary Fig. 6

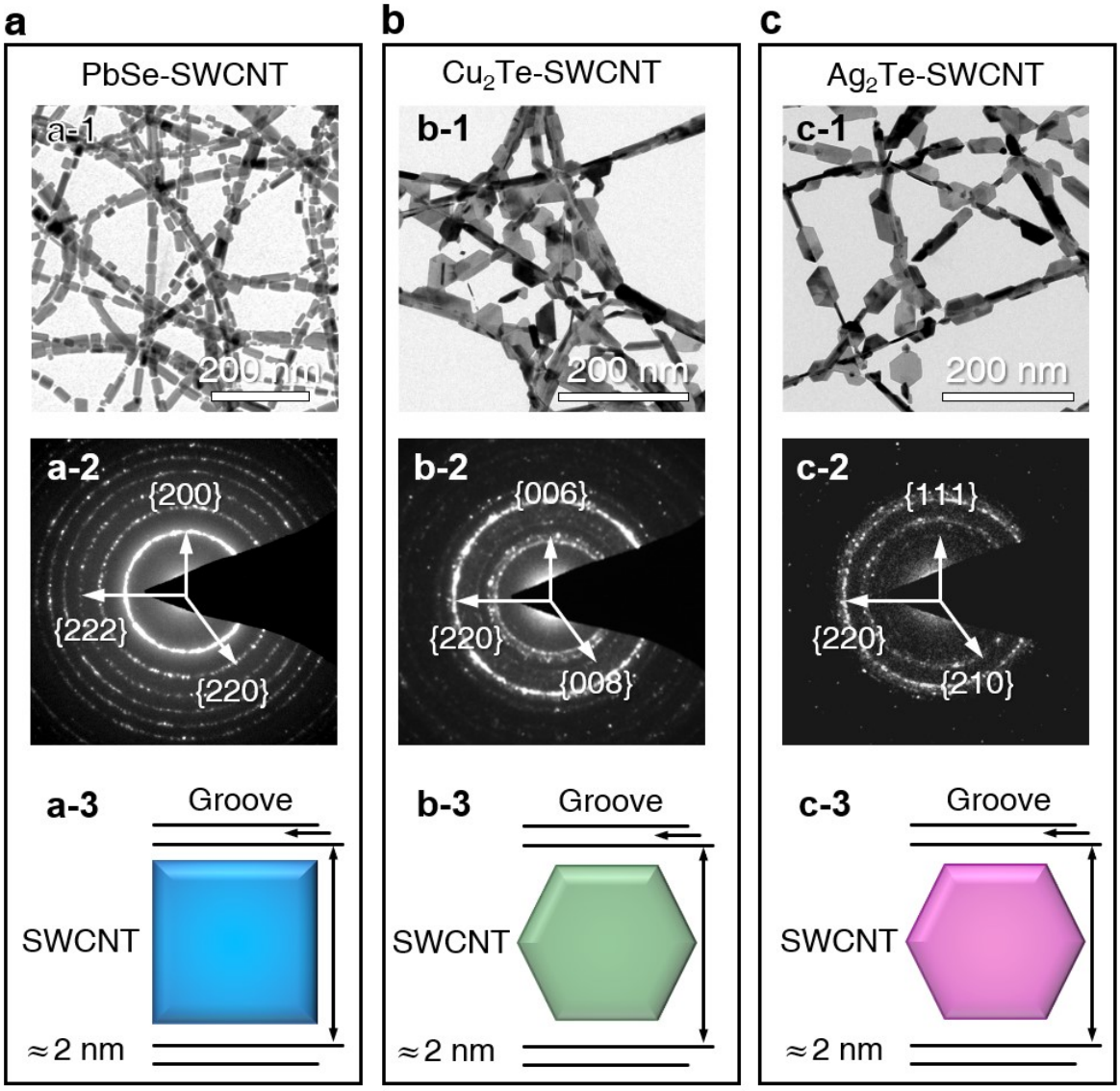

Supplementary Fig. 6 | Microstructural characterization of highly ordered SWCNT-PbSe, SWCNT-Cu_2Te and SWCNT-Ag_2Te hybrids. a, SWCNT-PbSe**, b,** SWCNT-Cu_2Te, **c,** SWCNT-Ag_2Te, Bright-field TEM images (**a-1**, **b-1**, **c-1**), the corresponding SAED patterns (**a-2**, **b-2**, **c-2**) and schematics of orientation relationships between the two components (**a-3**, **b-3**, **c-3**). Supplementary Fig. 6c-1 is also shown in Fig. 2a.

Supplementary Fig. 7

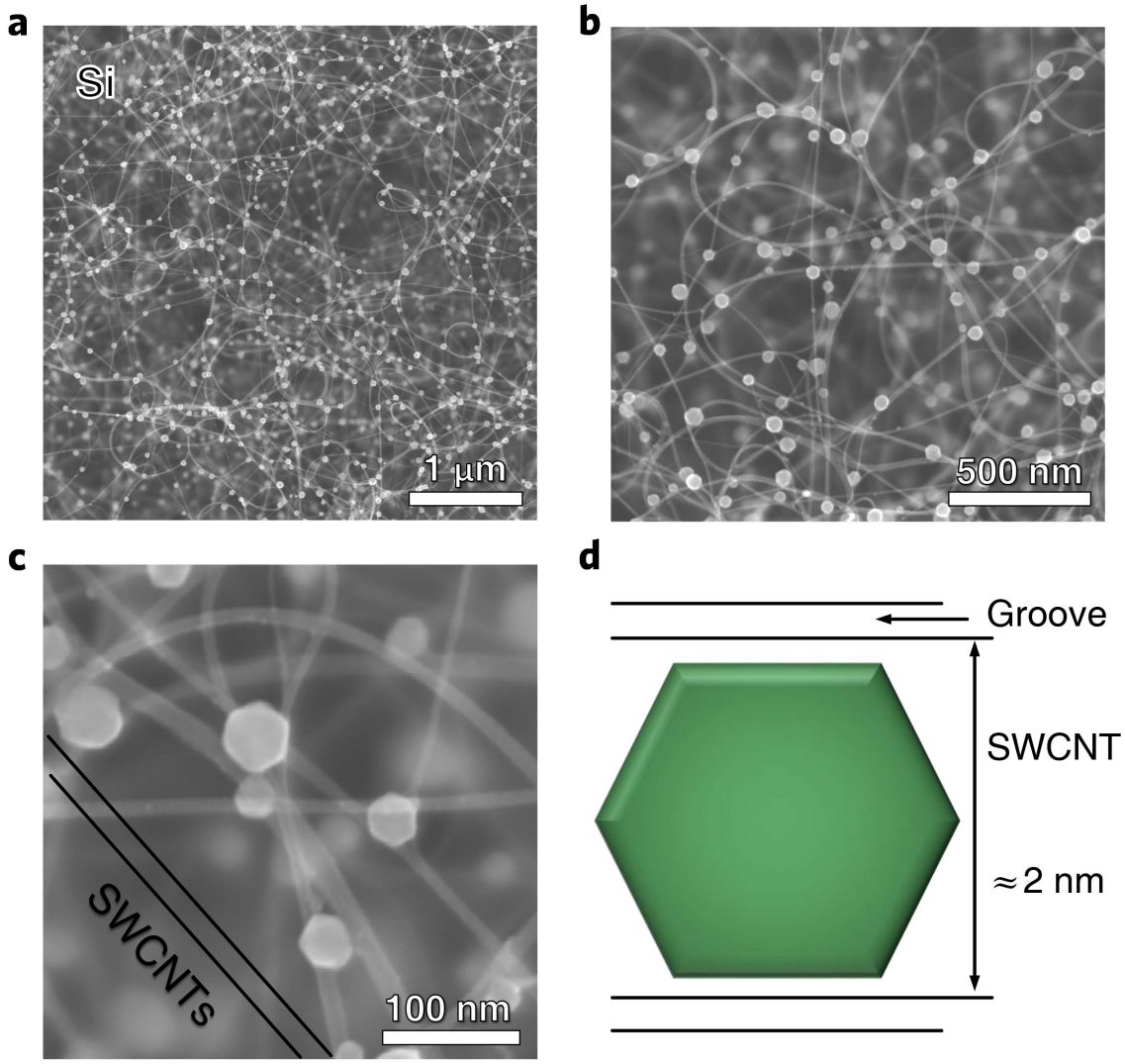

Supplementary Fig. 7 | Microstructural characterization of a highly ordered SWCNT-Si hybrid. **a-c**, SEM images. **d**, Schematic of the orientation relationship between the Si nanocrystal and a SWCNT.

Supplementary Fig. 8

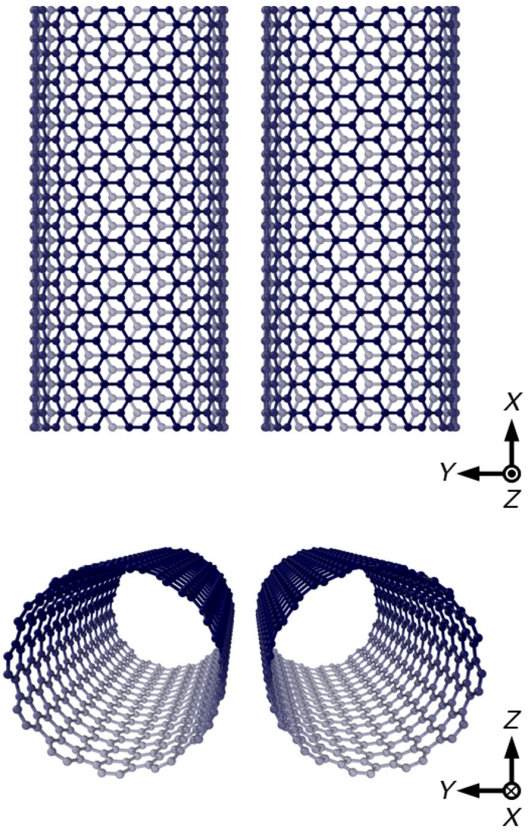

Supplementary Fig. 8 | Illustration of the structure of SWCNTs used in the computational simulation. Because the chiral angle of the SWCNTs has no obvious impact on the growth of the nanocrystal in our experimental results, all the SWCNTs used in simulations are armchair-type tubes.

Supplementary Fig. 9

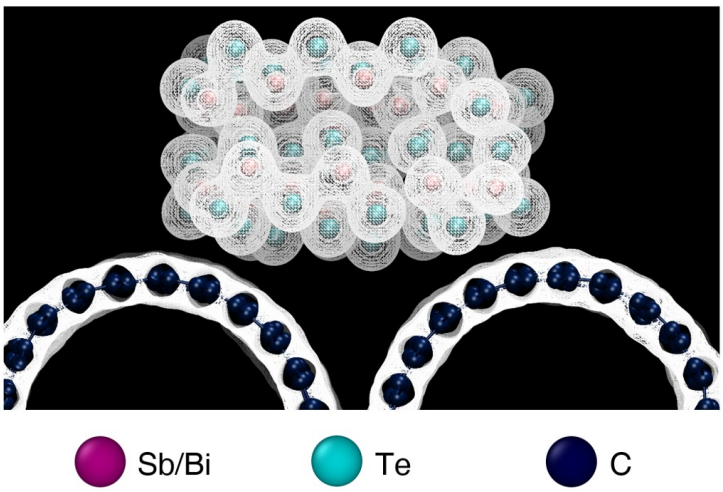

Supplementary Fig. 9 | The valence charge-density contour surface for a $(Bi,Sb)_2Te_3$ nanocrystal deposited on the groove region of a SWCNT bundle. The SWCNT-$(Bi,Sb)_2Te_3$ system is fully relaxed using the AIMD process. The white wireframe around the atoms is the isosurface of the valence charge-density. The strong overlap of the charge-density isosurface between metal atoms (Bi or Sb) and Te atoms indicates chemical bonding, while the empty black background between the $(Bi,Sb)_2Te_3$ nanocrystal and the SWCNT bundle shows no formation of chemical bonding between them.

475 **Supplementary Fig. 10**

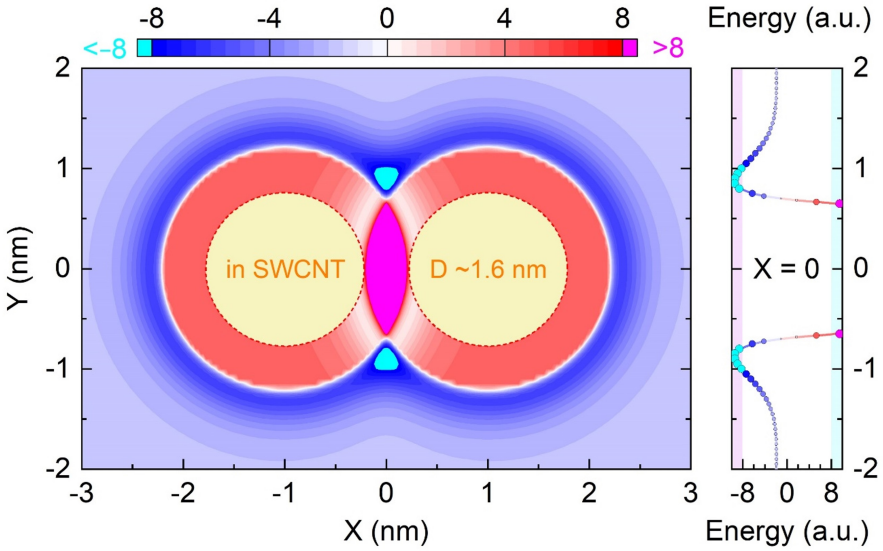

476

477 **Supplementary Fig. 10 | Schematic of the vdW interaction energy around SWCNTs.** The
478 SWCNT bundle groove has a stronger vdW force to guide an epitaxial growth than other areas.

Supplementary Fig. 11

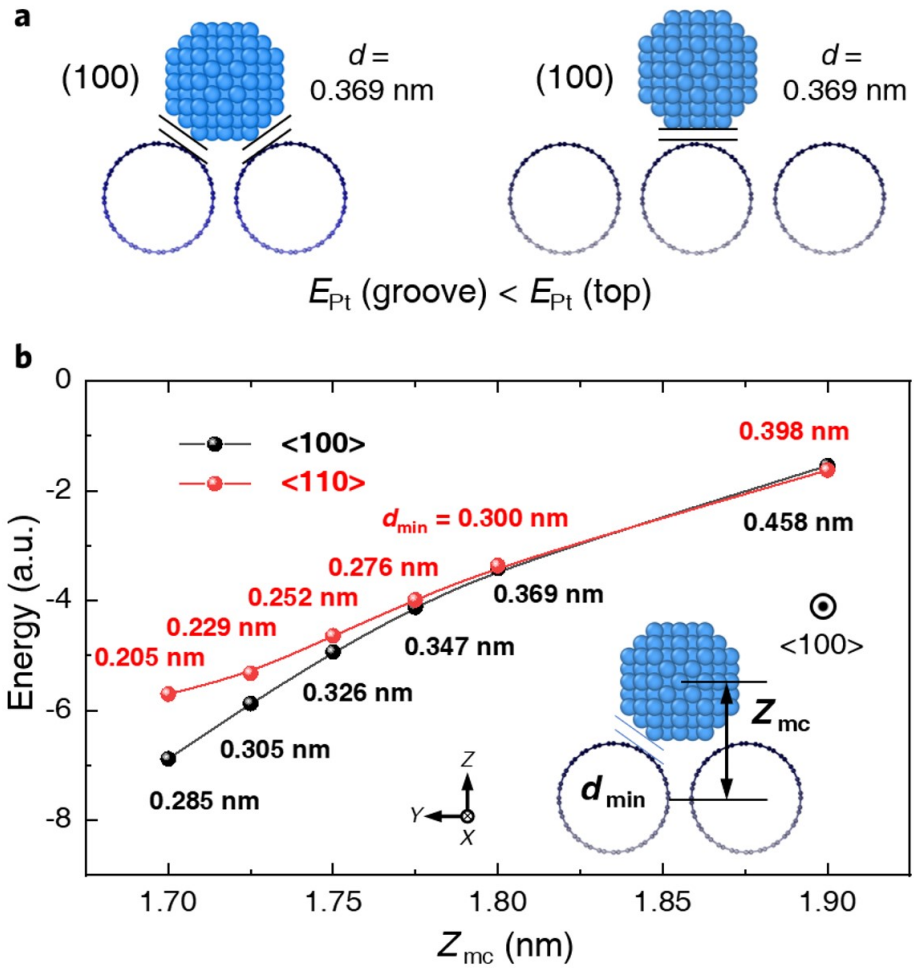

Supplementary Fig. 11 | Comparison of the calculated energy of a Pt nanocrystal with a truncated polyhedron shape with SWCNTs. a, Energy of Pt nanocrystals at the groove and other areas of SWCNTs. **b,** Energy of Pt nanocrystals at groove region with different orientations and positions. The Pt nanocrystal (100) atomic plane is parallel to the X-Y plane. Two sets of (100)-oriented Pt nanocrystals with <100> and <110> directions aligned with the SWCNT groove (X-axis) are calculated for the energy comparison. Inset: illustration of a SWCNT-Pt nanocrystal hybrid. Z_{mc} is the distance from the mass center of the Pt nanocrystal to the SWCNT. d_{min} is the minimum distance between the Pt nanocrystal and SWCNT atoms. d_{min} values are shown in the figure.

Supplementary Fig. 12

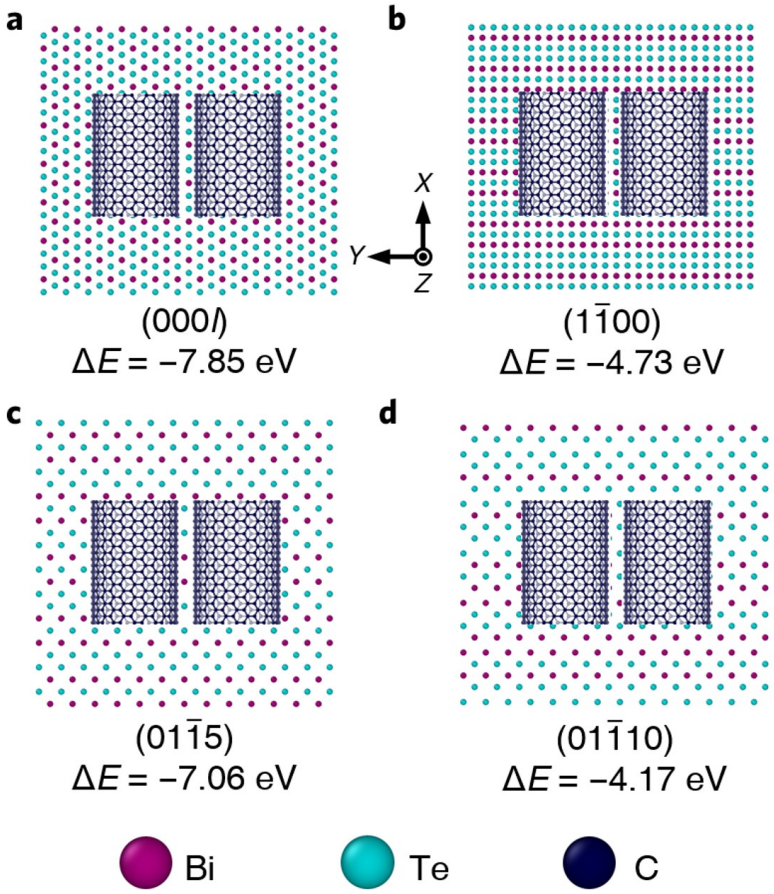

Supplementary Fig. 12 | Illustration of the calculated interface energy between different Bi_2Te_3 atomic planes and a SWCNT bundle. a, (000*l*)/SWCNT. **b,** (1$\bar{1}$00)/SWCNT. **c,** (01$\bar{1}$5)/SWCNT. **d,** (01$\bar{1}$10)/SWCNT. The interface energy is calculated by the formula: $\Delta E = E_{Bi_2Te_3\text{-SWCNT}} - (E_{CNT}+E_{Bi_2Te_3})$. The result clearly shows that the (000*l*) Bi_2Te_3 atomic plane/ SWCNT bundle has the minimum interface energy.

Supplementary Fig. 13

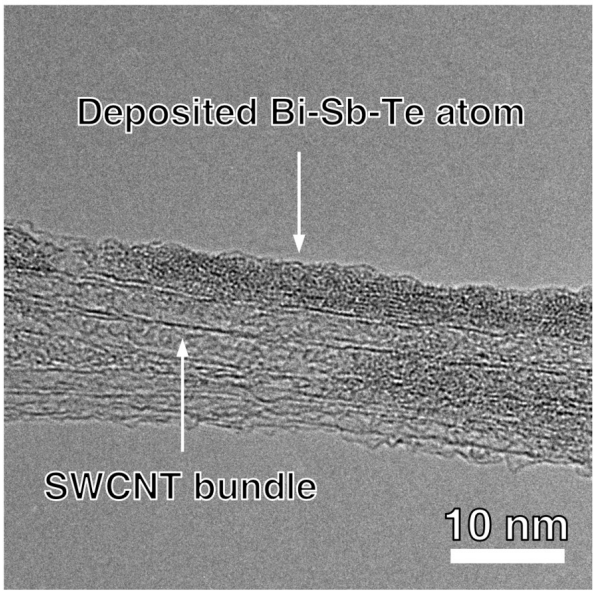

Supplementary Fig. 13 | Bright-field TEM image of Bi-Sb-Te atoms deposited on a SWCNT bundle.

Supplementary Fig. 14

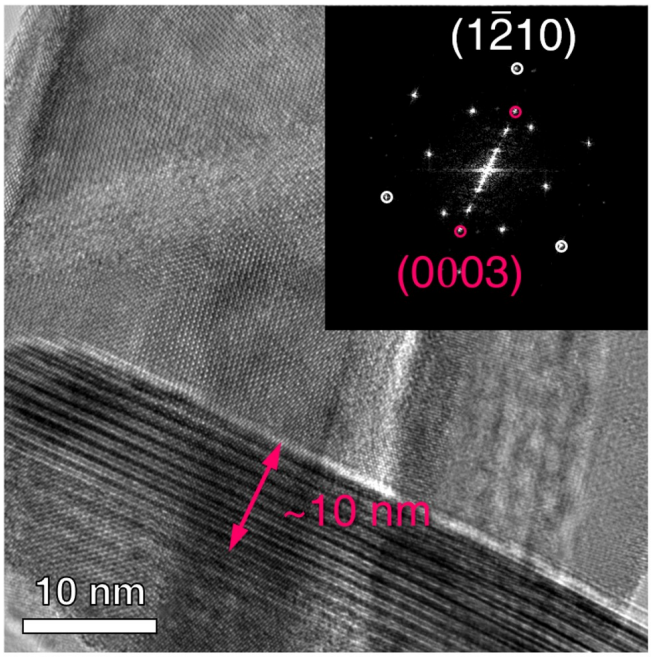

Supplementary Fig. 14 | Cross-sectional high magnification bright-field TEM image of a $(Bi,Sb)_2Te_3$ nanocrystal anchored on a SWCNT bundle. Inset is the corresponding FFT image.

Supplementary Fig. 15

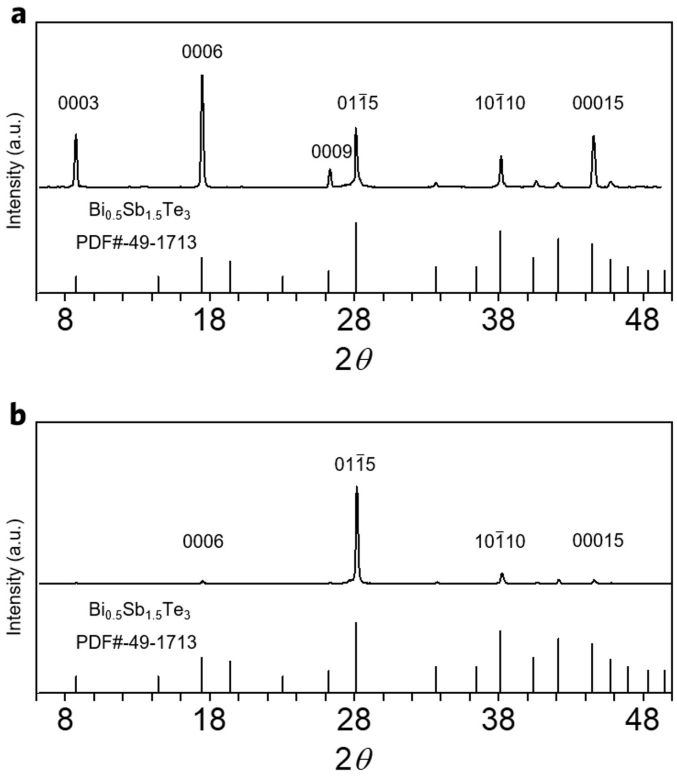

Supplementary Fig. 15 | X-ray diffraction (XRD) patterns of the SWCNT-$(Bi,Sb)_2Te_3$ hybrids. **a,** The (000*l*)-textured SWCNT-$Bi_{0.5}Sb_{1.5}Te_3$ hybrid. **b**, the non-(000*l*)-textured SWCNT-$Bi_{0.5}Sb_{1.5}Te_3$ hybrid.

Supplementary Fig. 16

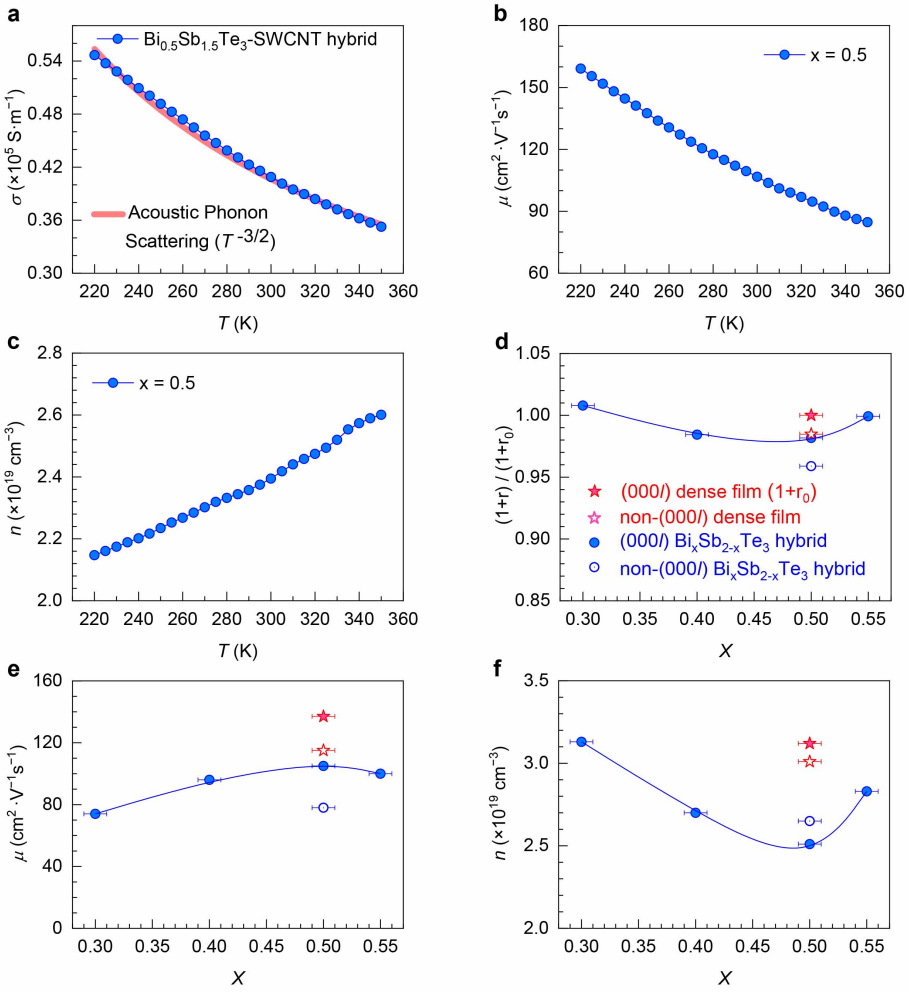

Supplementary Fig. 16 | Measurement of electrical properties of SWCNT-$(Bi,Sb)_2Te_3$ hybrids and a $(Bi,Sb)_2Te_3$ dense film. a, Temperature-dependent electrical conductivity. **b,** Carrier mobility. **c,** Carrier concentration. **d,** Bi-doping concentration-dependent relative $m^*(1+r)$ values. **e,** Carrier mobility. **f,** Carrier concentration.

Supplementary Fig. 17

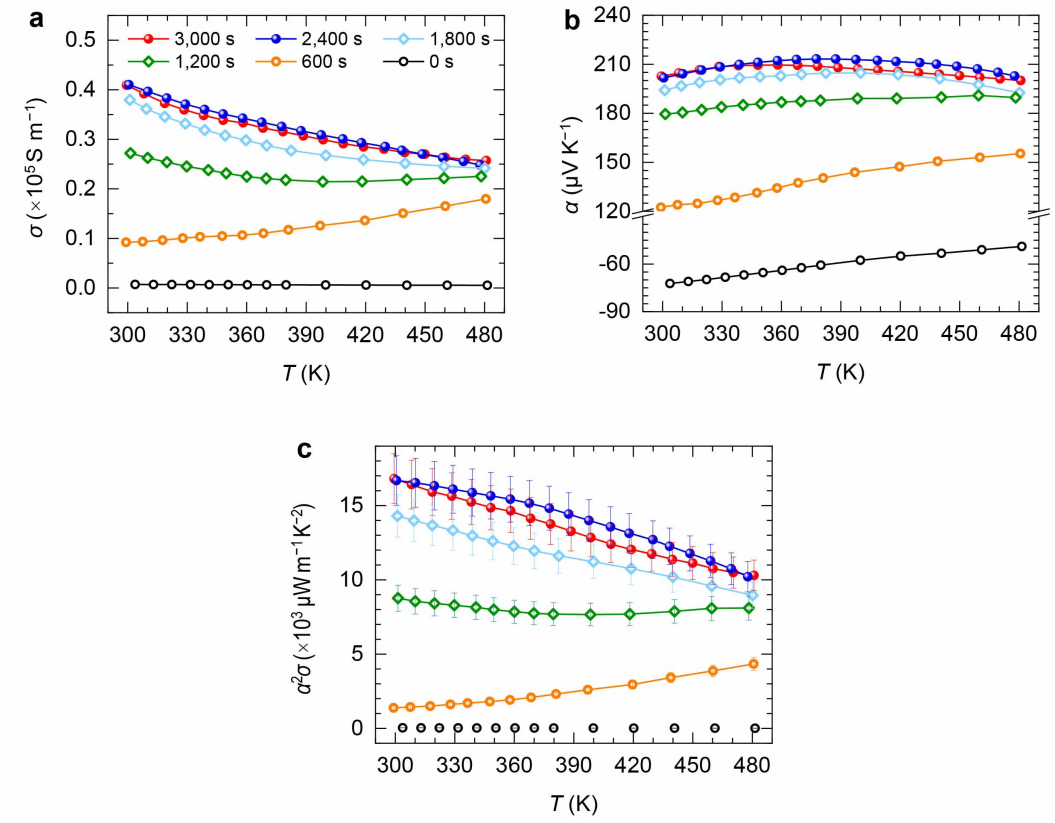

Supplementary Fig. 17 | TE properties of the (000*l*)-textured SWCNT-$Bi_{0.5}Sb_{1.5}Te_3$ hybrid with different $Bi_{0.5}Sb_{1.5}Te_3$ deposition times. a, Electrical conductivity. **b**, Seebeck coefficient. **c**, Power factor, its measurement uncertainty is about 10%.

Supplementary Fig. 18

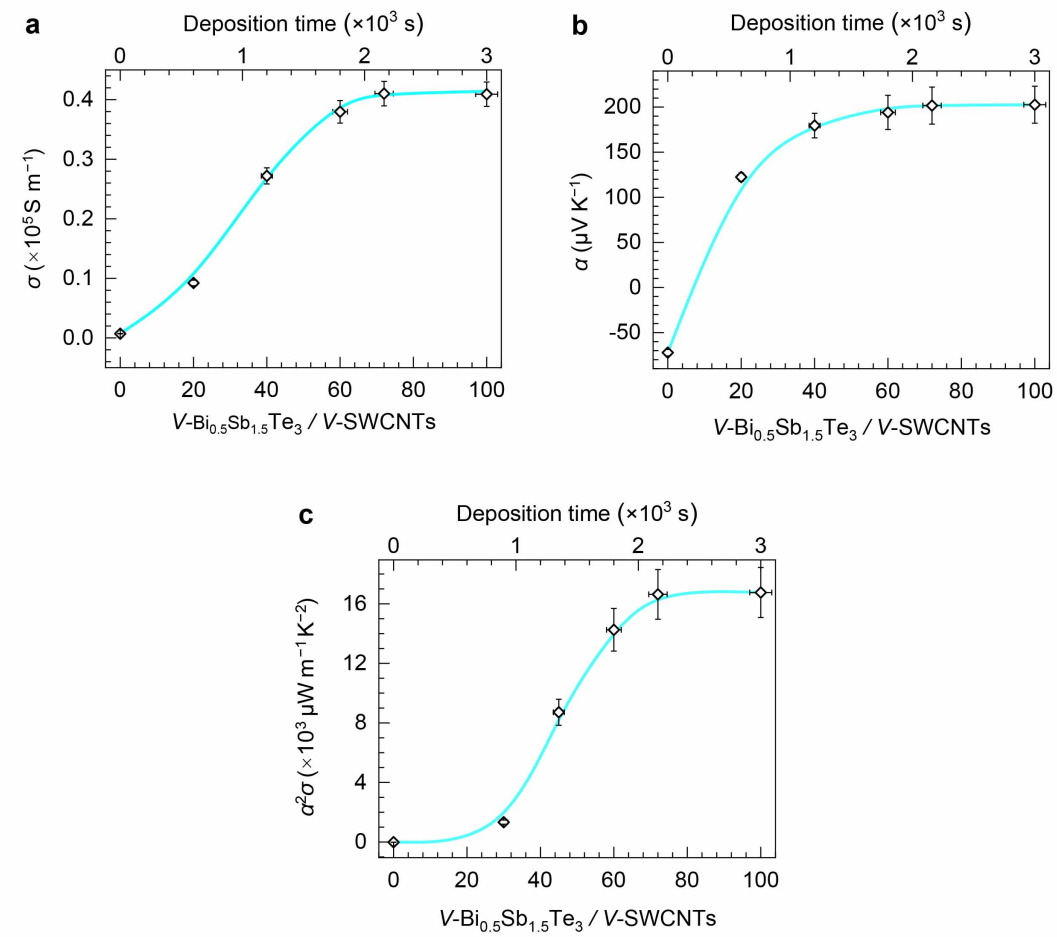

Supplementary Fig. 18 | Dependence of the room temperature TE performances of (000*l*)-textured SWCNT-$Bi_{0.5}Sb_{1.5}Te_3$ hybrids on the $Bi_{0.5}Sb_{1.5}Te_3$ deposition time ($Bi_{0.5}Sb_{1.5}Te_3$ volume ratios, *V*- $Bi_{0.5}Sb_{1.5}Te_3$/*V*-SWCNT). **a**, Electrical conductivity. **b**, Seebeck coefficient. **c**, Power factor. The respective measurement uncertainties for **a**-**c** are about 5%, 3% and 10%.

Supplementary Fig. 19

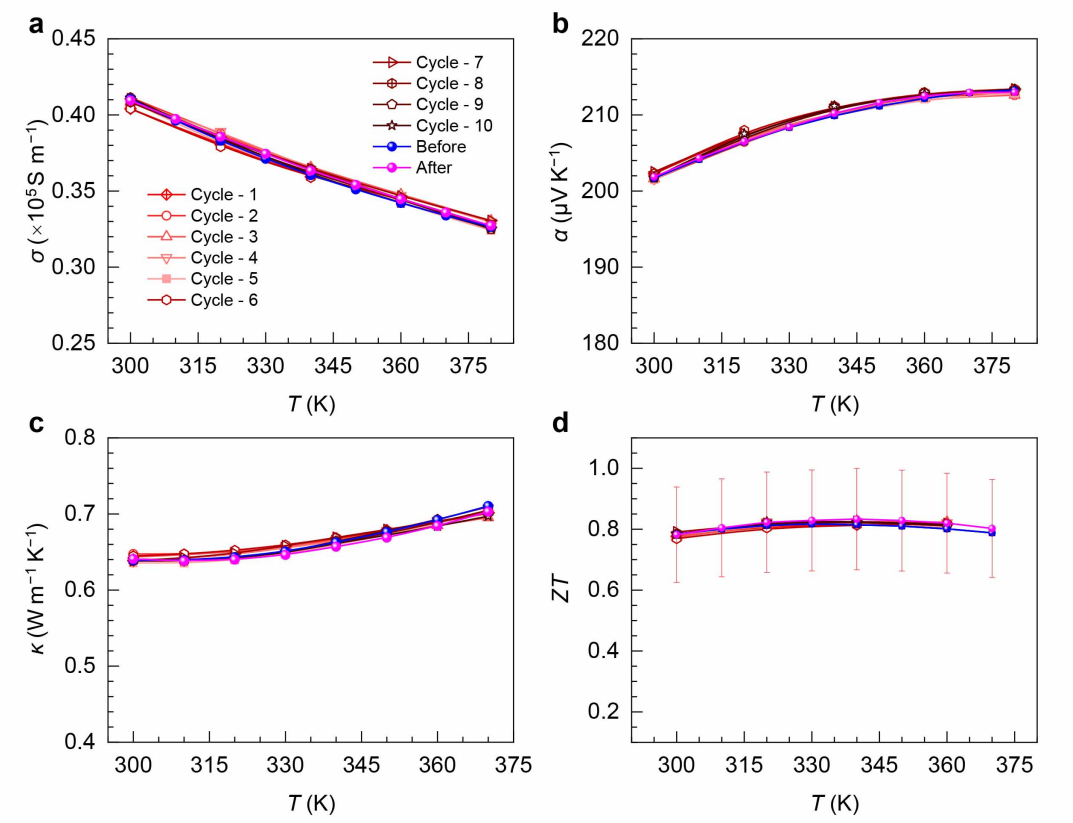

Supplementary Fig. 19 | TE performance stability test of a 720-nm-thick (000*l*)-textured SWCNT-$Bi_{0.5}Sb_{1.5}Te_3$ hybrid. a, Electrical conductivity. **b**, Seebeck coefficient. **c**, Thermal conductivity. **d**, Calculated *ZT* value. The respective measurement uncertainties for **a**-**d** are about 5%, 3%, 10% and 20%.

Supplementary Fig. 20

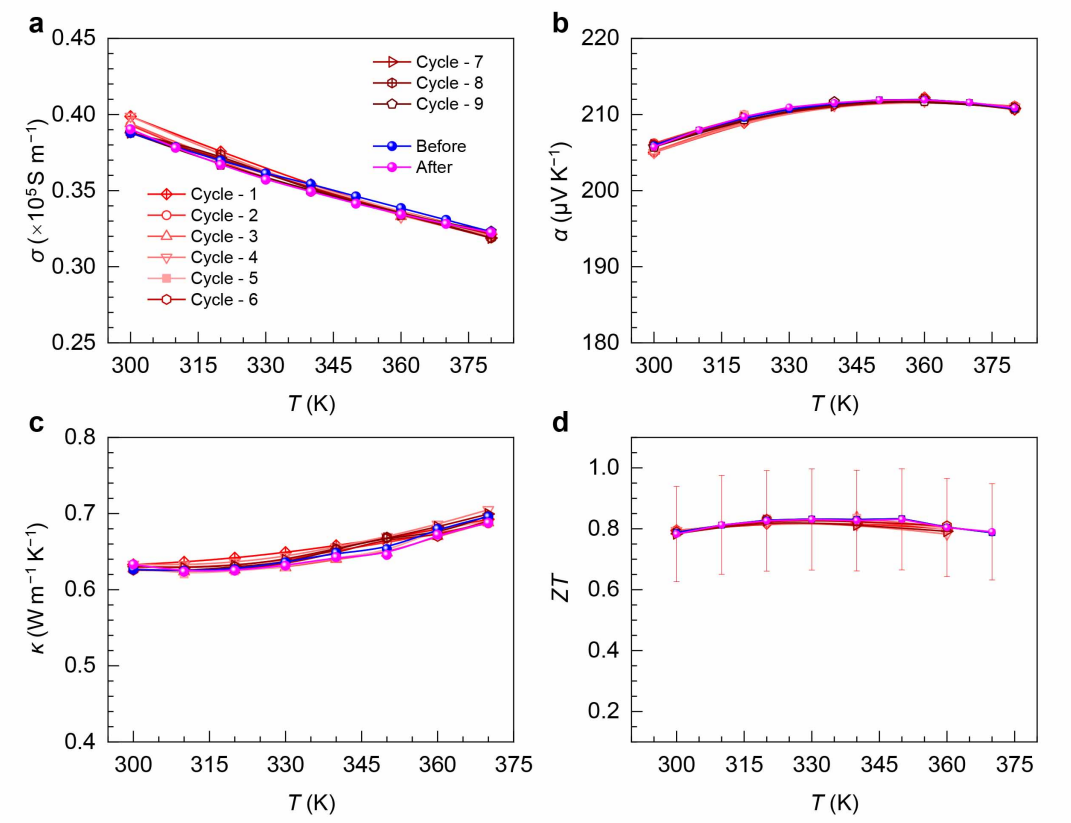

Supplementary Fig. 20 | TE performance stability test of a 720-nm-thick (000*l*)-textured SWCNT-$Bi_{0.5}Sb_{1.5}Te_3$ hybrid. a, Electrical conductivity. **b**, Seebeck coefficient. **c**, Thermal conductivity. **d**, Calculated *ZT* value. The respective measurement uncertainties for **a**-**d** are about 5%, 3%, 10% and 20%.

Supplementary Fig. 21

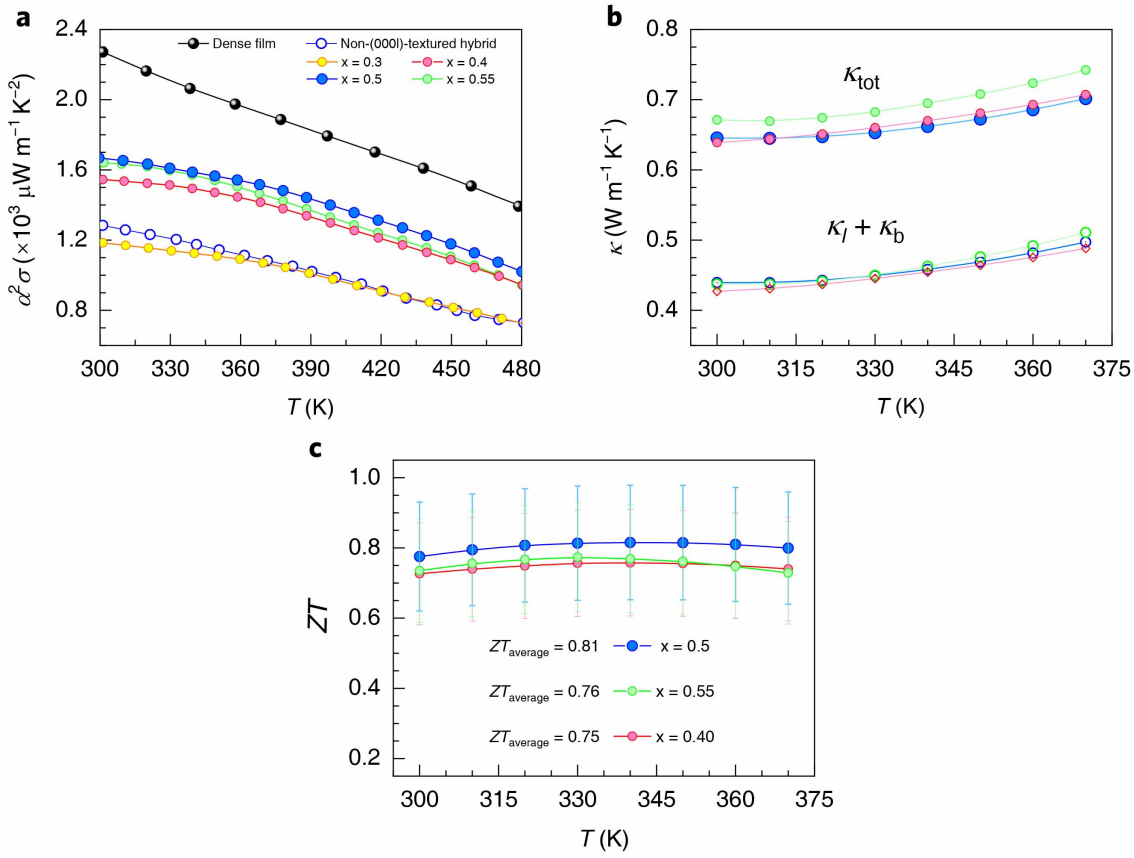

Supplementary Fig. 21 | Thermoelectric characterization of the (000*l*)-textured SWCNT-$Bi_xSb_{2-x}Te_3$-hybrid, a (000*l*)-textured dense $Bi_{0.5}Sb_{1.5}Te_3$ film and a non-(000*l*)-textured SWCNT-$Bi_{0.5}Sb_{1.5}Te_3$ hybrid. a, Calculated power factors, **b**, Total in-plane thermal conductivity and contributions from lattice thermal conductivity and a bipolar effect, **c**, Calculated ZT values. Error bars for the calculated *ZT* are ~20%, as determined from the measurement uncertainties in the Seebeck coefficient (~3%), electrical conductivity (~5%) and thermal conductivity (~10%).

Supplementary Fig. 22

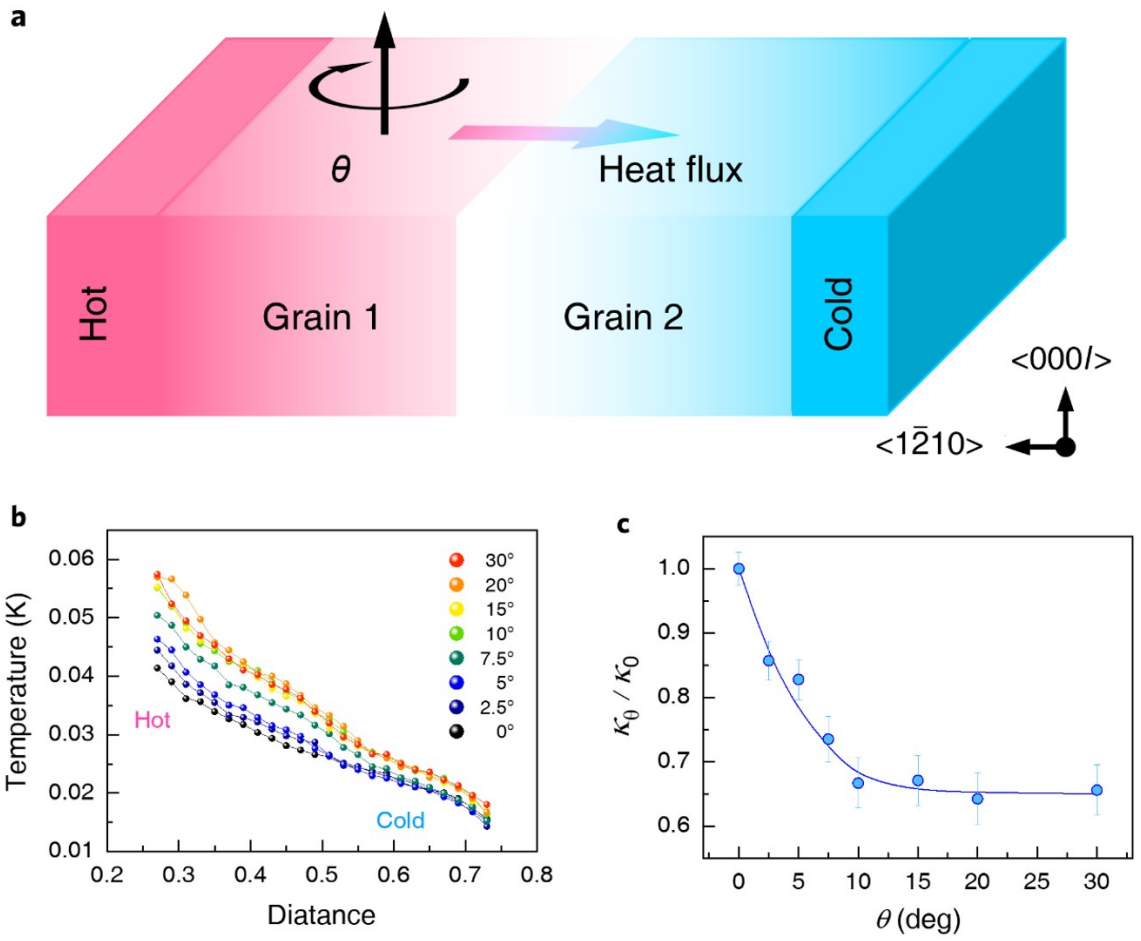

Supplementary Fig. 22 | The influence of tilt boundaries with different angles (θ) on the thermal conductivity of a Sb_2Te_3 nanocrystal. a, Illustration of heat conduction across neighboring nanocrystals with a tilt boundary. **b**, Illustration of the temperature gradients of nanocrystals after full relaxation. The thermal conductivity (κ) is inversely proportional to the value of ΔT. The result shows that the κ value rapidly decreases with the increase of tilt angle from 0° to 10° and then slowly decreases from 10° to 30°. **c**, Thermal conductivity of two Sb_2Te_3 nanocrystals with a tilt boundary.

Supplementary Fig. 23

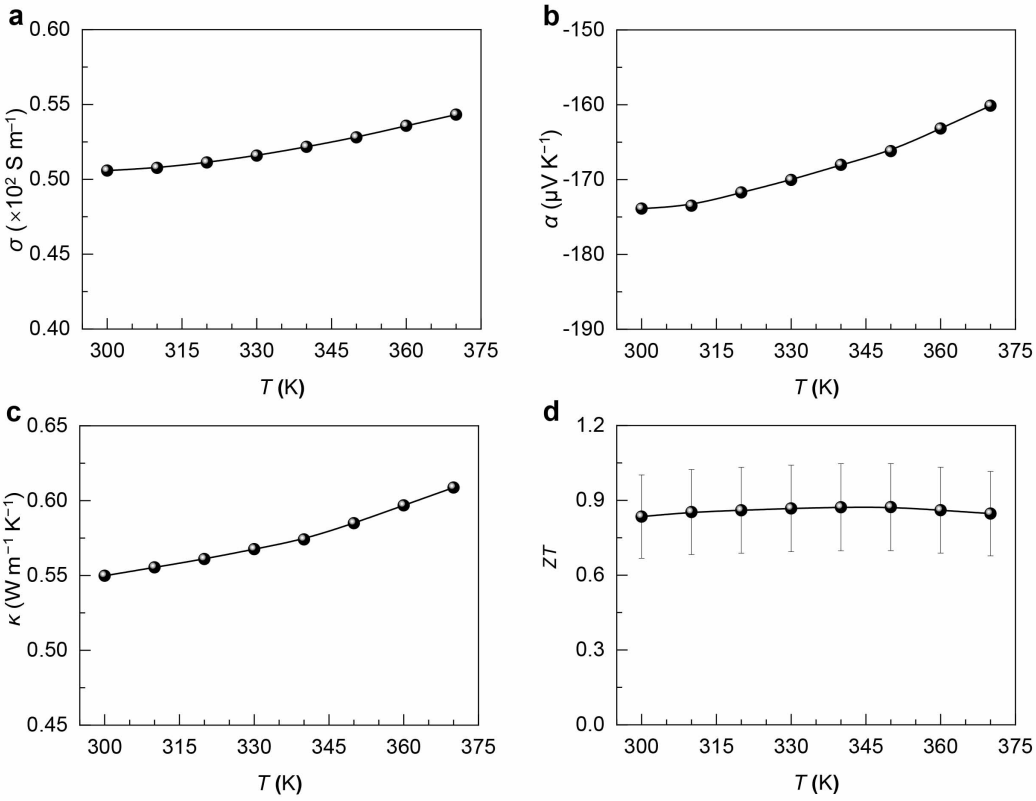

Supplementary Fig. 23 | TE properties of the n-type SWCNT-Bi_2Te_3 hybrid. a, Electrical conductivity**. b,** Seebeck coefficient. **c**, Thermal conductivity. **d**, Calculated *ZT* value. The Error bar of calculated *ZT* is ~± 20%.

Supplementary Fig. 24

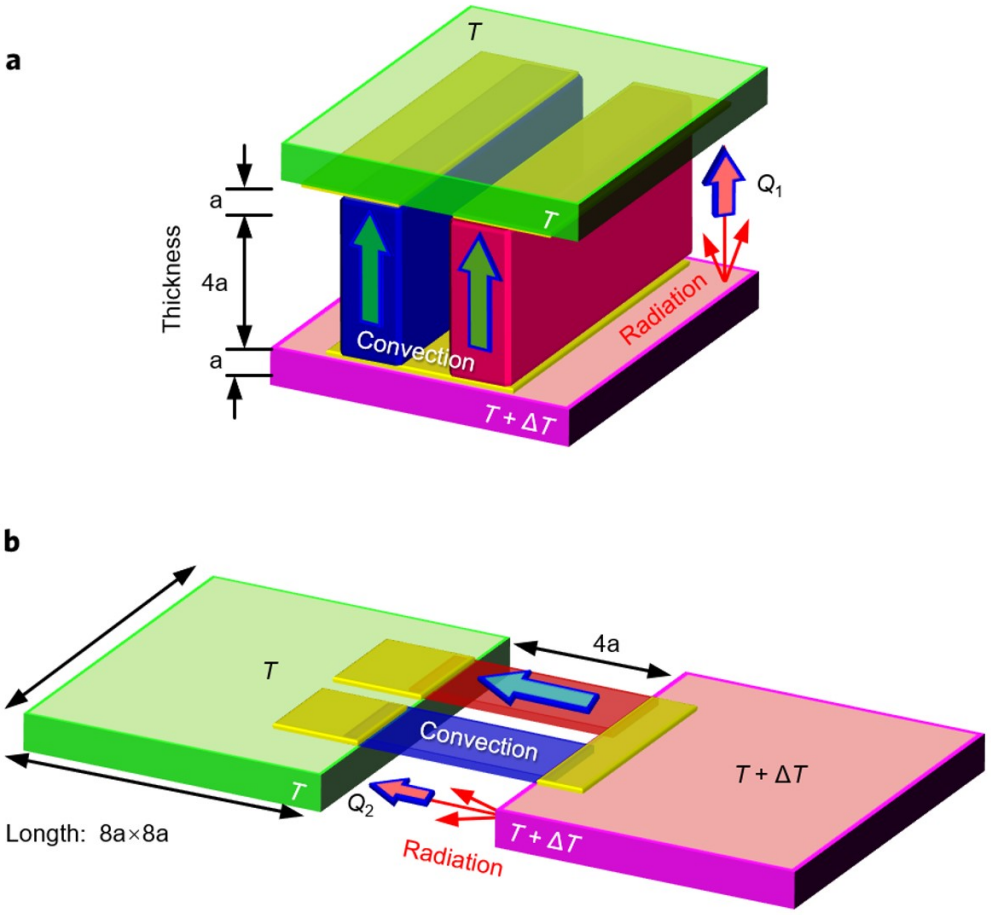

Supplementary Fig. 24 | Illustration of direct radiative and convective heat transfer between the heat source and heat sink. Comparison of TEDs with a vertical structure (**a**) and a lateral structure (**b**).

Supplementary Fig. 25

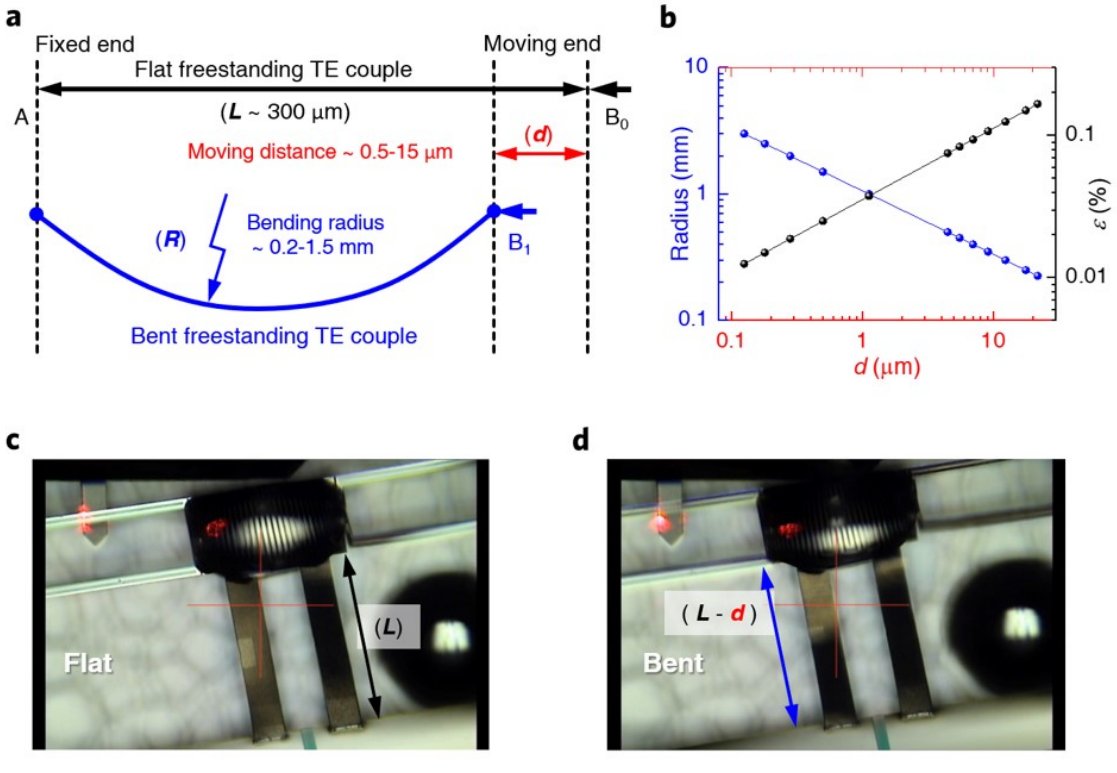

Supplementary Fig. 25 | Flexibility evaluation of a freestanding p-n couple of a micro-TED by an AFM instrument. **a**, Schematic of the bending a freestanding p-n couple driven by an AFM probe. **b**, Dependence of the bending radius of curvature (R) and the strain (ε) of the freestanding p-n couple on the distance moved (d). **c**, **d** are the photographs of the flat and bent freestanding p-n couple.

Supplementary Fig. 26

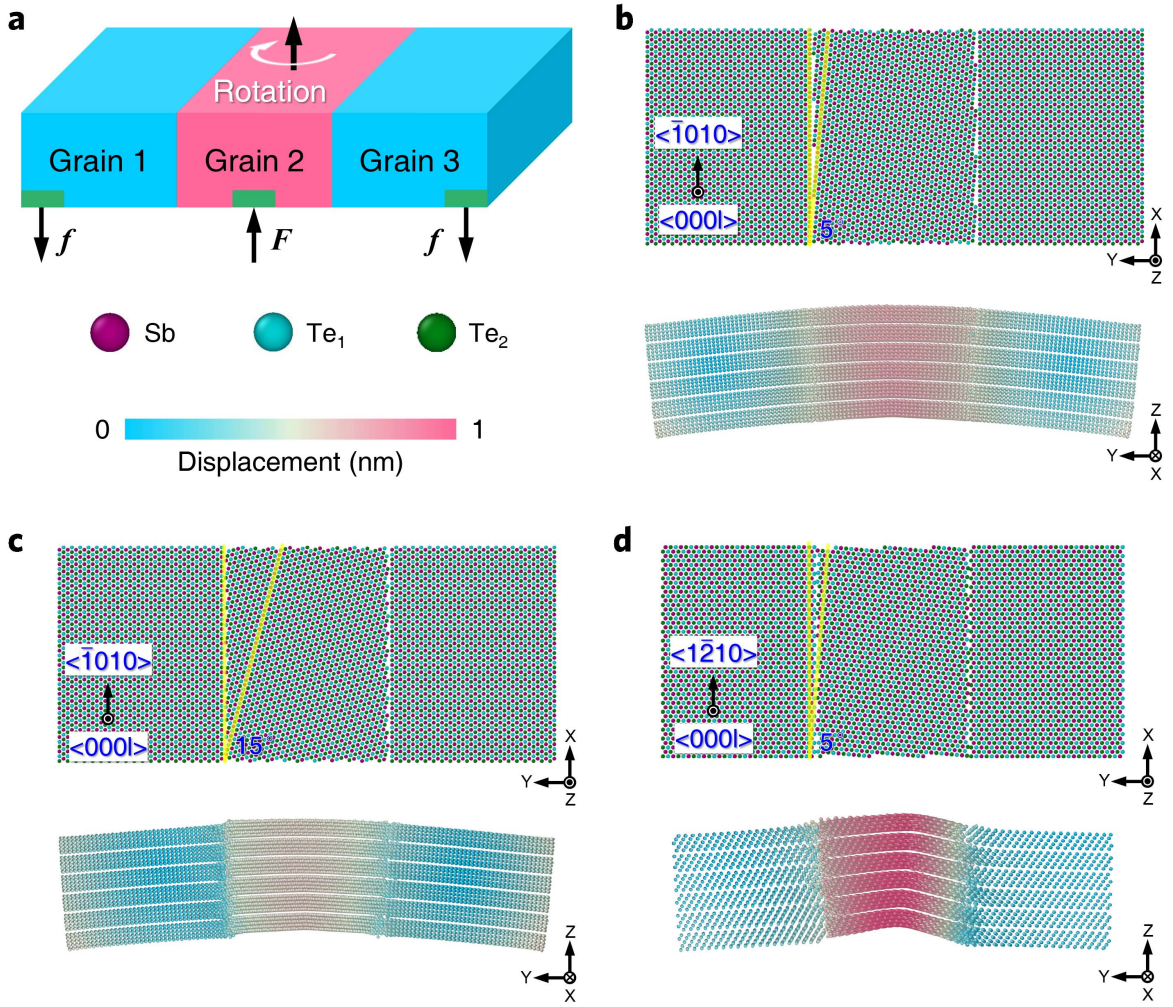

Supplementary Fig. 26 | MD simulation of Sb_2Te_3 nanocrystals under bending. **a**, Illustration of the three-point model used for MD simulation. Sb_2Te_3 nanocrystals with low 5° (**b**) and high 15° (**c**) angle tilt boundaries along Sb_2Te_3 <1$\bar{2}$10> direction, and low 5° (**d**) angle tilt boundaries along Sb_2Te_3 <1$\bar{1}$00> direction. The (000*l*) atomic planes of Sb_2Te_3 nanocrystals are parallel to the X-Y plane before bending simulations. The atomic displacement and shear strain of each case under bending deformation are shown on the Y-Z plane.

Supplementary Table 1 | Calculated orientation factors F(X) of the SWCNT-$(Bi,Sb)_2Te_3$ hybrids

(*X*)	0006	$01\bar{1}5$	$10\bar{1}10$	00015
000*l*	0.3483	−0.3253	−0.1467	0.0952
non-000*l*	0.0051	0.7487	−0.1358	−0.0468

Supplementary References

1. Baughman, R. H., Zakhidov, A. A. & de Heer, W. A. Carbon nanotubes-the route toward applications. *Science* **297,** 787-793 (2002).
2. Kharlamova, M. V. Electronic properties of pristine and modified single-walled carbon nanotubes. *PHYS-USP+* **56,** 1047-1073 (2013).
3. Feng, C., Wang, J., Cheng, Y., He, P. & Liew, K. M. Diffusion mechanism of platinum nanoclusters on well-aligned carbon nanotubes. *RSC Adv.* **4,** 60711-60719 (2014).
4. Hutter, J., Iannuzzi, M., Schiffmann, F. & VandeVondele, J. cp2k: atomistic simulations of condensed matter systems. *WIREs Comput. Mol. Sci.* **4,** 15-25 (2014).
5. Plimpton, S. Fast parallel algorithms for short-range molecular dynamics. *J. Comput. Phys.* **117,** 1-19 (1995).
6. Kresse, G. & Furthmüller, J. Efficiency of ab-initio total energy calculations for metals and semiconductors using a plane-wave basis set. *Comput. Mater. Sci.* **6,** 15-50 (1996).
7. Tuckerman, M. E. Ab initiomolecular dynamics: basic concepts, current trends and novel applications. *J. Phys. Condens. Matter* **14,** R1297-R1355 (2002).
8. Roy Chowdhury, P., Feng, T. & Ruan, X. Development of interatomic potentials for the complex binary compound Sb_2Te_3 and the prediction of thermal conductivity. *Phys. Rev. B* **99,** 155202 (2019).
9. Dahal, A. & Batzill, M. Graphene–nickel interfaces: a review. *Nanoscale* **6,** 2548-2562 (2014).
10. Mishra, S. K., Satpathy, S. & Jepsen, O. Electronic structure and thermoelectric properties of bismuth telluride and bismuth selenide. *J. Phys. Condens. Matter* **9,** 461-470 (1997).
11. Jin, Q.*, et al.* Flexible layer-structured Bi_2Te_3 thermoelectric on a carbon nanotube scaffold. *Nat. Mater.* **18,** 62-68 (2019).
12. Mu, X.*, et al.* Enhanced electrical properties of stoichiometric $Bi_{0.5}Sb_{1.5}Te_3$ film with high-crystallinity via layer-by-layer in-situ growth. *Nano Energy* **33,** 55-64 (2017).
13. Liao, H.-G.*, et al.* Facet development during platinum nanocube growth. *Science* **345,** 916-919 (2014).
14. Lotgering, F. K. Topotactical reactions with ferrimagnetic oxides having hexagonal crystal structure. *J. Inorg. Nucl. Chem.* **9,** 113-123 (1959).
15. Kim, Y.*, et al.* Structural and thermoelectric transport properties of Sb_2Te_3 thin films grown by molecular beam epitaxy. *J. Appl. Phys.* **91,** 715-718 (2001).
16. Zhao, Y.*, et al.* Decoupling phonon and carrier scattering at carbon nanotube/Bi_2Te_3 interfaces for improved thermoelectric performance. *Carbon* **170,** 191-198 (2020).
17. Gong, J. J.*, et al.* Investigation of the bipolar effect in the thermoelectric material $CaMg_2Bi_2$ using a first-principles study. *PCCP* **18,** 16566-16574 (2016).
18. Collins, P. G., Bradley, K., Ishigami, M. & Zettl, A. Extreme oxygen sensitivity of electronic properties of carbon nanotubes. *Science* **287,** 1801-1804 (2000).
19. Faleev, S. V. & Léonard, F. Theory of enhancement of thermoelectric properties of materials with nanoinclusions. *Phys. Rev. B* **77,** 214304 (2008).
20. Martin, J., Wang, L., Chen, L. & Nolas, G. S. Enhanced Seebeck coefficient through energy-barrier scattering in PbTe nanocomposites. *Phys. Rev. B* **79,** 115311 (2009).
21. Kim, M., Freeman, A. J. & Geller, C. B. Screened exchange LDA determination of the ground and excited state properties of thermoelectrics: Bi_2Te_3. *Phys. Rev. B* **72,** 035205 (2005).
22. Snyder, G. J. & Toberer, E. S. Complex thermoelectric materials. *Nat. Mater.* **7,** 105-114 (2008).
23. Cutler, M., Leavy, J. F. & Fitzpatrick, R. L. Electronic transport in semimetallic cerium sulfide. *Phys.*

Rev. **133,** A1143-A1152 (1964).
24. Larson, P., Mahanti, S. D. & Kanatzidis, M. G. Electronic structure and transport of Bi_2Te_3 and $BaBiTe_3$. *Phys. Rev. B* **61,** 8162-8171 (2000).
25. Zheng, Y.*, et al.* Mechanically robust BiSbTe alloys with superior thermoelectric performance: a case study of stable hierarchical nanostructured thermoelectric materials. *Adv. Energy Mater.* **5,** 1401391 (2015).
26. Hu, L. P.*, et al.* Shifting up the optimum figure of merit of p-type bismuth telluride-based thermoelectric materials for power generation by suppressing intrinsic conduction. *NPG Asia Mater.* **6,** e88 (2014).
27. Zhang, Q.*, et al.* Constructing nanoporous carbon nanotubes/Bi_2Te_3 composite for synchronous regulation of the electrical and thermal performances. *J. Appl. Phys.* **121,** 055104 (2017).
28. Kim, H. S., Gibbs, Z. M., Tang, Y., Wang, H. & Snyder, G. J. Characterization of Lorenz number with Seebeck coefficient measurement. *APL Mater.* **3,** 105 (2015).
29. Takashiri, M., Tanaka, S. & Miyazaki, K. Improved thermoelectric performance of highly-oriented nanocrystalline bismuth antimony telluride thin films. *Thin Solid Films* **519,** 619-624 (2010).
30. Schumacher, C.*, et al.* Optimizations of pulsed plated p and n-type Bi_2Te_3-based ternary compounds by annealing in different ambient atmospheres. *Adv. Energy Mater.* **3,** 95-104 (2013).
31. Wang, Y. G., Qiu, B., H., M. A. J., Xiulin, R. & Xianfan, X. Mode-wise thermal conductivity of bismuth telluride. *J. Heat Transfer* **135,** 091102 (2013).
32. Fang, T.*, et al.* Complex band structures and lattice dynamics of Bi_2Te_3-based compounds and solid solutions. *Adv. Funct. Mater.* **29,** 1900677 (2019).
33. Qiao, J.*, et al.* Tailoring nanoporous structures in Bi_2Te_3 thin films for improved thermoelectric performance. *ACS Appl. Mater. Interfaces* **11,** 38075-38083 (2019).
34. Wirnsberger, P., Frenkel, D. & Dellago, C. An enhanced version of the heat exchange algorithm with excellent energy conservation properties. *J. Chem. Phys.* **143,** 124104 (2015).
35. Rowe, D. M. *Thermoelectrics Handbook: Macro to Nano* (CRC, Boca Raton, 2006).
36. Suo, Z., Ma, E. Y., Gleskova, H. & Wagner, S. Mechanics of rollable and foldable film on foil electronics. *Appl. Phys. Lett.* **74,** 1177-1179 (1999).
37. Huang, B. L. & Kaviany, M. Ab initio and molecular dynamics predictions for electron and phonon transport in bismuth telluride. *Phys. Rev. B* **7720,** 125209 (2008).
38. Jenkins, J. O., Rayne, J. A. & Ure, R. W. Elastic moduli and phonon properties of Bi_2Te_3. *Phys. Rev. B* **5,** 3171 (1972).
39. Huang, J.*, et al.* Polyimide/POSS nanocomposites: interfacial interaction, thermal properties and mechanical properties. *Polymer* **44,** 4491-4499 (2003).
40. Oikawa, E., Motomi, K. & Aoki, T. Synthesis and properties of polyimide-clay hybrid films. *J. Polym. Sci., Part A: Polym. Chem.* **35,** 2493-2498 (1997).